Mouse ANKRD31 Regulates Spatiotemporal Patterning of Meiotic Recombination Initiation and Ensures Recombination between X and Y Sex Chromosomes

Frantzeskos Papanikos, Julie a J Clément, Erika Testa, Ramya Ravindranathan, Corinne Grey, Ihsan Dereli, Anastasiia Bondarieva, Sarai Valerio-Cabrera, Marcello Stanzione, Alexander Schleiffer, et al.

ANKRD31 regulates spatiotemporal patterning of meiotic recombination initiation and ensures recombination between heterologous sex chromosomes in mice

Authors

Frantzeskos Papanikos[1‡], Julie A.J. Clément[2‡], Erika Testa[3], Ramya Ravindranathan[1], Corinne Grey[2], Ihsan Dereli[1], Anastasiia Bondarieva[1], Sarai Valerio-Cabrera[1], Marcello Stanzione[1,9], Alexander Schleiffer[5,6], Petr Jansa[4], Diana Lustyk[4], Ji-Feng Fei[7], Ian R. Adams[8], Jiri Forejt[4], Marco Barchi[3], Bernard de Massy[2*], Attila Toth[1*π]

Affiliations

[1] Institute of Physiological Chemistry, Faculty of Medicine, Technische Universität Dresden, Fetscherstraße 74, 01307 Dresden, Germany

[2] Institute of Human Genetics, UMR 9002, CNRS, Université de Montpellier, 34396 Montpellier cedex 5, France

[3] Department Biomedicine and Prevention, Faculty of Medicine, University of Rome Tor Vergata, Via Montpellier n.1, 00133, Rome, Italy

[4] Institute of Molecular Genetics, Division BIOCEV, Prumyslova 595, 25250 Vestec, Czech Republic

[5] Research Institute of Molecular Pathology (IMP), Campus-Vienna-Biocenter 1, Vienna BioCenter (VBC), 1030 Vienna, Austria

[6] Institute of Molecular Biotechnology (IMBA), Dr. Bohr-Gasse 3, Vienna BioCenter (VBC), 1030 Vienna, Austria

[7] Institute for Brain Research and Rehabilitation, South China Normal University, 510631, Guangzhou, China

[8] MRC Human Genetics Unit, MRC Institute of Genetics and Molecular Medicine, University of Edinburgh, Western General Hospital, Edinburgh, EH4 2XU, United Kingdom

[9] Current address: Massachusetts General Hospital Cancer Center, Harvard Medical School, Charlestown, Massachusetts 02129, USA

E-mails:

frantzeskos.papanikos@mailbox.tu-dresden.de

julie.clement@igh.cnrs.fr
corinne.grey@igh.cnrs.fr
erikatesta87@gmail.com
ihsan.dereli@mailbox.tu-dresden.de
ramya.ravindranathan@tu-dresden.de
Anastasiia.Bondarieva@mailbox.tu-dresden.de
sarai.valerio_cabrera@tu-dresden.de
MSTANZIONE@mgh.harvard.edu
pjansa@img.cas.cz
diana.lustyk@img.cas.cz
jiri.forejt@img.cas.cz
Alexander.Schleiffer@imp.ac.at
jifeng.fei@imp.ac.at
Ian.Adams@igmm.ed.ac.uk

marco.barchi@uniroma2.it
bernard.de-massy@igh.cnrs.fr
attila.toth@mailbox.tu-dresden.de
‡ Equal contribution to work
*Correspondence to bernard.de-massy@igh.cnrs.fr and attila.toth@mailbox.tu-dresden.de
π Lead author

Summary

Orderly segregation of chromosomes during meiosis requires that crossovers form between homologous chromosomes by recombination. Programmed DNA double-strand breaks (DSBs) initiate meiotic recombination. We identify ANKRD31 as a key component of complexes of DSB-promoting proteins which assemble on meiotic chromosome axes. Genome-wide, ANKRD31 deficiency causes delayed recombination initiation. In addition, loss of ANKRD31 alters DSB distribution owing to reduced selectivity for sites that normally attract DSBs. Strikingly, ANKRD31 deficiency also abolishes uniquely high rates of recombination that normally characterize pseudoautosomal regions (PARs) of X and Y chromosomes. Consequently, sex chromosomes do not form crossovers leading to chromosome segregation failure in ANKRD31-deficient spermatocytes. These defects co-occur with a genome-wide delay in assembling DSB-promoting proteins on autosome axes and a loss of a specialized PAR-axis domain that is highly enriched for DSB-promoting proteins in wild-type. Thus, we propose a model for spatiotemporal

patterning of recombination by ANKRD31-dependent control of axis-associated DSB-promoting proteins.

Introduction

Programmed DNA double-strand breaks (DSBs) are critical for meiosis, as they initiate meiotic homologous recombination, and their repair generates reciprocal DNA exchanges, called crossovers (CO). In most organisms, COs must form between each pair of homologous chromosomes (homologs) for correct chromosome segregation in the first meiotic division (Hunter, 2015). Due to the importance and the potential genotoxicity of DSBs, DSB formation and repair are under tight spatiotemporal control (Keeney et al., 2014).

Meiotic DSB formation and repair take place within the context of the meiosis-specific chromosome axis and the synaptonemal complex (SC), reviewed in (de Massy, 2013; Hunter, 2015; Keeney et al., 2014). Initially, multiple DSBs are formed along the axes, which are linear chromatin structures along the shared core of sister chromatid pairs in meiotic prophase. Single-stranded DNA ends formed by processing of DSBs invade homologs, which promotes alignment and synapsis of homolog axes. It is the resultant SC where recombination completion, including CO formation, occurs.

DSB formation is catalyzed by an evolutionary conserved topoisomerase-like enzyme complex, consisting of the SPO11 enzyme and its binding partner TOPOVIBL (Bergerat et al., 1997; Keeney et al., 1997; Robert et al., 2016; Vrielynck et al., 2016). SPO11 activity depends on a partially conserved set of auxiliary proteins, MEI4, REC114 and IHO1 in mice, which assemble into axis-bound complexes, called pre-DSB recombinosomes, prior to DSB formation (de Massy, 2013; Kumar et al., 2010; Stanzione et al., 2016). Pre-DSB recombinosomes are thought to promote DSBs by activating SPO11 on axes. Anchoring of pre-DSB recombinosomes to axes relies on IHO1 (Mer2 in budding yeast) and meiosis-specific HORMA-domain proteins in both budding yeast and mammals (Kumar et al., 2015; Kumar et al., 2018; Panizza et al., 2011; Stanzione et al., 2016). HORMAD1-IHO1 assemblies can form independent of MEI4 or REC114 thereby providing an axis-bound platform for pre-DSB recombinosome assembly (Kumar et al., 2018; Stanzione et al., 2016). HORMAD1, IHO1 and pre-DSB recombinosomes are restricted to unsynapsed axes, which is hypothesized to concentrate DSB forming activity to genomic regions requiring DSBs for completion of homolog alignment (Kauppi et al., 2013; Stanzione et al., 2016; Wojtasz et al., 2009).

Meiotic chromatin is thought to be arrayed into loops anchored on chromosome axes (Zickler and Kleckner, 1999) and DSBs seem to form in these loops (Blat et al., 2002; Panizza et al., 2011). Sites of frequent DSB formation, called hotspots, are also associated with open chromatin marks, such as trimethylation of histone H3 lysine 4 (H3K4me3) and lysine 36 (H3K36me3) (Buard et al., 2009; Davies et al., 2016; Grey et al., 2017; Powers et al., 2016; Smagulova et al., 2011). Thus, axis-bound pre-DSB recombinosomes are hypothesized to target SPO11 activity by recruiting open chromatin sites from within loops to the axis via a poorly understood mechanism, reviewed in (Grey et al., 2018). In most mammals, DSB hotspots emerge at sites bound by the histone methyltransferase PRDM9 in a sequence specific manner. PRDM9 generates the histone marks H3K4me3 and H3K36me3 at these sites (Grey et al., 2018). Additionally, by an unknown mechanism, PRDM9 prevents DSBs at other H3K4me3-rich genomic locations such as transcription start sites or enhancers, which serve as hotspots in *Prdm9*$^{-/-}$ meiocytes (hereafter called default hotspots) (Brick et al., 2012; Diagouraga et al., 2018). An exception to this rule is the pseudoautosomal region (PAR) of X and Y chromosomes, where high DSB activity occurs independently of PRDM9 (Brick et al., 2012). X and Y chromosomes are homologous only in the PAR, therefore at least one CO must form in this relatively short region to ensure segregation of these chromosomes. Thus, DSB density is between 10 to 110 fold higher in the PAR than the rest of the genome (Kauppi et al., 2011; Lange et al., 2016). High DSB activity is possibly enabled by a unique PAR-chromatin environment characterized by both strong accumulation of PRDM9-independent histone H3K4me3 (Brick et al., 2012), and the combination of a disproportionately long axis and short chromatin loops (Kauppi et al., 2011). However, the importance of these features in DSB control has not been tested, and mechanisms underlying high recombination rate in the PAR remain enigmatic.

Here we report the identification of a novel meiotic protein, ANKRD31, which plays a major role in the temporal and spatial control of meiotic DSBs. Strikingly, ANKRD31 is required to prevent DSBs at default hotspot sites, and to ensure DSBs/COs in the PAR. Both roles likely rely on ANKRD31´s function in organizing axis-bound pre-DSB recombinosomes.

Results

Conserved ANKRD31 associates with pre-DSB recombinosomes

To identify new players in meiotic recombination we searched for genes that are preferentially expressed in mouse gonads where prophase meiocytes are present. We reviewed ENCODE

transcriptome datasets (Consortium, 2011, 2012) and profiled expression in reproductive tissues. This approach identified a previously uncharacterized gene, *Ankrd31* (Figure 1A, 1B and 1SA). *Ankrd31* encodes a 1857 amino acid protein (XP_006517860) that is conserved among vertebrates (Figure 2S). In most vertebrate taxa, ANKRD31 contains two separated triplets of Ankyrin repeats, which are common protein-protein interaction motifs (Mosavi et al., 2004). C-terminal to the Ankyrin repeats there are three further conserved domains, a predicted coiled-coil domain and two regions without functional predictions.

Immunostaining of histological sections of testes reconfirmed presence of ANKRD31 in meiotic cells (Figure 1C and S1B). Antibodies to both an N- and a C-terminal fragment of ANKRD31 stained spermatocyte nuclei from premeiotic DNA replication until early pachytene. In contrast, somatic cells lacked a consistent ANKRD31 signal. Localization of ANKRD31 was analyzed in detail in nuclear surface spread spermatocytes at distinct prophase sub-stages (Figure 1D and Table S1, see STAR Methods for staging prophase). Focal ANKRD31 staining was detected on chromatin between preleptotene and early pachytene with focus numbers peaking in leptotene (Figure 1D-G and S1C-F). Most ANKRD31 foci associated with the chromosome axes (85.5% in leptotene, n=29, and 88.7% in early zygotene, n=32, spermatocytes), but foci were depleted from axes upon SC formation (Figure 1E, S1C and S1E). Beyond numerous relatively small foci (median diameter, 0.26 µm), ANKRD31 also formed up to eight larger aggregates (median diameter 0.62 µm) from preleptotene to pachytene (Figure 1D, 1F and S1F). Median numbers of aggregates peaked at five in leptotene and declined to three as spermatocytes progressed to early pachytene (n=108 spermatocytes). ANKRD31 localization resembled the localization of two pre-DSB recombinosome components, MEI4 and REC114 (Kumar et al., 2010; Kumar et al., 2015; Stanzione et al., 2016). We found substantial colocalization between ANKRD31 and MEI4 or REC114 foci (Figure 2A-F, S3A), and large ANKRD31 aggregates always colocalized with similar aggregates of REC114 (n=98 spermatocytes) and MEI4 (n=89 spermatocytes and n=24 oocytes, Figure 2A, 2D, 2G and 3SA-C) in both sexes.

Yeast two-hybrid (Y2H) assays also indicated that ANKRD31 directly interacted with two known components of pre-DSB recombinosomes, IHO1 and REC114, but not with HORMAD1 (Figure 2H, S3D and Table S2), which acts as an anchor for pre-DSB recombinosomes on axes (Kumar et al., 2015; Stanzione et al., 2016). These results suggest that ANKRD31 might be incorporated into pre-DSB recombinosomes by directly interacting with REC114 and IHO1.

ANKRD31 forms aggregates in PARs

We examined ANKRD31 aggregates closer, because aggregates of pre-DSB recombinosome components were poorly characterized before. In zygotene and pachytene, where chromosome axes were well developed, it was apparent that aggregates of ANKRD31, REC114 and MEI4 associated with the ends of a subset of chromosomes (Figure 1D, 1F, 2G S3B and S3C). In spermatocytes, one of the aggregates always associated with PARs of X and Y chromosomes. The rest of the aggregates were associated with up to three non-centromeric autosomal ends (Figure S1F). Consistent with these observations, an independent study by Acquaviva et al. 2019 discovered that the presence of similar sequences in PARs and the non-centromeric ends of autosome 4, 9 and 13 is associated with ANKRD31 aggregate formation at these loci in both oocytes and spermatocytes. Peculiarly, whereas ANKRD31, MEI4, and REC114 foci were detectable only on unsynapsed axes, aggregates persisted on synapsed chromosome ends till early pachytene, which was most obvious in PARs in spermatocytes (Figure 1D, 1F, 2G and S3B-C). Aggregates disappeared only after meiocytes progressed beyond early pachytene (Figure 1D and not shown).

Distinct molecular requirements for ANKRD31 aggregates and foci

Given their differential persistence in synapsed regions, foci and aggregates of ANKRD31/MEI4/REC114 might represent qualitatively different protein complexes with distinct underlying molecular requirements. To test this possibility we compared localization of ANKRD31, REC114 and MEI4 in *Mei4*$^{-/-}$, *Rec114*$^{-/-}$ and *Iho1*$^{-/-}$ spermatocytes (Figure 2J and S3E-I). Previously, strongly reduced REC114 and MEI4 focus numbers were reported in *Mei4*$^{-/-}$ and *Rec114*$^{-/-}$ mice, respectively (Kumar et al., 2018). In addition, we found that both focus and aggregate formation of ANKRD31, REC114 and MEI4 were each disrupted in *Mei4*$^{-/-}$ and *Rec114*$^{-/-}$ spermatocytes (Figure S3E-G and Table S3). Remarkably, only ANKRD31 (Figure 2I), MEI4 and REC114 foci (Stanzione et al., 2016), but not aggregates, were diminished in *Iho1*$^{-/-}$ spermatocytes (Figure 2J). ANKRD31 aggregates formed efficiently in *Iho1*$^{-/-}$ spermatocytes; median numbers of aggregates were four in both wild type (n=62) and *Iho1*$^{-/-}$ (n=57) spermatocytes in zygotene. These aggregates always colocalized with aggregates of MEI4 (n=100) and REC114 (n=100) in *Iho1*$^{-/-}$ spermatocytes (Figure 2J and S3H). ANKRD31 aggregates also colocalized with PAR FISH signals in late zygotene-like *Iho1*$^{-/-}$ spermatocytes (≥94% of FISH signals and ANKRD31 aggregates colocalize with each other, n=51) (Figure S3I). These observations support the hypothesis that ANKRD31 interacts with MEI4/REC114 complexes. Furthermore, these data show that distinct molecular requirements underpin focus formation of ANKRD31, MEI4 and REC114 in non-PAR regions and aggregate formation of the

same proteins in PARs and at PAR-like ends of chromosome 4, 9 and 13 (as identified by (Acquaviva et al., 2019).

Loss of ANKRD31 affects fertility of mice

To test ANKRD31´s functions we generated two mouse lines (by CRISPR/Cas9 editing) with distinct frameshift mutations in exon 6 of *Ankrd31* (Figure 3A). These lines had indistinguishable phenotypes in initial analysis, hence, we focused only on one of them, mut1. A frameshift after the 134th codon in the longest open reading frame (ORF) of *Ankrd31*, is predicted to severely truncate ANKRD31 in the mut1 line. Hence, we refer to mut1 as a loss of function allele (*Ankrd31*$^{-/-}$) hereafter. Immunoprecipitation-western blot analysis of testis extracts and immunofluorescence in fixed gonadal samples reconfirmed that ANKRD31 domains which are C-terminal to the frameshift position are not produced in *Ankrd31*$^{-/-}$ meiocytes (Figure S4A-F). Disruption of *Ankrd31* caused no obvious somatic phenotypes but led to fertility defects. Whereas female *Ankrd31*$^{-/-}$ mice were fertile, they lost fertility faster than wild-type in advanced age. Average numbers of pups/breeding week were 1.53 and 1.38 between 8-28 weeks of age (not significant), and 0.92 and 0.45 beyond 28 weeks of age (p=0.0272, paired t-test) in wild-type and *Ankrd31*$^{-/-}$ mothers, respectively (n=6 mice for each genotype). Male *Ankrd31*$^{-/-}$ mice were infertile (no pups after 88 breeding weeks, n=5 males).

To test if these fertility defects were caused by a reduced capacity of *Ankrd31*$^{-/-}$ meiocytes to progress through meiosis, we examined oocytes and spermatocytes in histological sections. Consistent with reduced female fertility, we observed 4.95 fold lower median oocyte numbers in *Ankrd31*$^{-/-}$ mice than wild-type at 6-7 weeks of age (Figure S4G). This reduction in oocyte number was associated with elevated rates of apoptosis, as determined by cleaved PARP1 staining (Daniel et al., 2011; Ghafari et al., 2007), in the oocytes of newborn *Ankrd31*$^{-/-}$ mice as compared to wild-type (Figure S4H). Consistent with a loss of fertility in males, testis weight was 2.7 fold lower in *Ankrd31*$^{-/-}$ than wild-type mice (Figure S4I). Investigation of gametogenesis in histological sections revealed elevated apoptosis after mid pachytene in spermatocytes of *Ankrd31*$^{-/-}$ mice (Figure S4J and Table S4). Nevertheless, noticeable fractions of spermatocytes progressed to the first meiotic metaphase, where they arrested, which was evidenced by the elevated proportion of seminiferous tubules that contained metaphase cells (Figure 3B and 3C). These metaphase cells often contained chromosomes that did not line up at the metaphase plate (1.7% and 89% in n=173 and n=146 wild type and Ankrd31$^{-/-}$ meiotic metaphase I spermatocytes, respectively), which indicated chromosome alignment defects in *Ankrd31*$^{-/-}$ mice (Figure 3B). Most metaphase spermatocytes underwent apoptosis and only few post-meiotic cells were detected in *Ankrd31*$^{-/-}$ mice (Figure S4J).

We conclude that compromised meiocyte survival provides a plausible explanation for fertility defects in *Ankrd31*$^{-/-}$ mice.

Compromised synapsis in *Ankrd31*$^{-/-}$ meiocytes

Persistent DSBs and defective synapsis induce oocyte elimination in newborn mice and spermatocyte elimination in pachytene (Barchi et al., 2005; Burgoyne et al., 2009; Di Giacomo et al., 2005). In contrast, deficiencies in maturation of DSBs into COs lead to chromosome alignment defects and an arrest in metaphase I in spermatocytes (Burgoyne et al., 2009). Hence, the complex patterns of elimination of *Ankrd31*$^{-/-}$ meiocytes prompted us to investigate meiotic recombination in *Ankrd31*$^{-/-}$ mice. Both chromosome axis formation and SC formation are used to stage meiotic prophase and provide a reference for kinetic studies of recombination (Table S1). Hence, we tested firstly if chromosome axis, and secondly if SC form with normal kinetics in *Ankrd31*$^{-/-}$ spermatocytes. Axes formed with wild type kinetics (Figure S5A), but SC formation was delayed on autosomes in *Ankrd31*$^{-/-}$ spermatocytes (Figure 3D and 3E). Despite this delay most *Ankrd31*$^{-/-}$ spermatocytes seemed to complete autosomal SC formation in adults (Figure 3D). Due to methodological limitations it is unclear if all spermatocytes succeeded in autosomal synapsis in adults (see STAR Methods for explanation). Autosomal SC formation occurred with high fidelity as we did not observe obvious non-homologous interactions in pachytene stage spermatocytes (n>200) in our *Ankrd31*$^{-/-}$ mutant line. SC formation was compromised in *Ankrd31*$^{-/-}$ oocytes (Figure S5B), which also manifested in higher rates of asynapsis in *Ankrd31*$^{-/-}$ oocytes (54.76%, n=126 oocyte) than wild type oocytes (22.96%, n=135 oocyte) at a fetal developmental stage where oocytes are in mid pachytene (Table S5). Together, these observations suggest that whereas ANKRD31 is not required for homology search *per se*, ANKRD31 is required for efficient and timely engagement of homologous chromosomes genome wide in both sexes.

Compared to autosomes, we observed a more penetrant defect in SC formation between the PARs of the heterologous sex chromosomes in males. PARs failed to synapse in 99.7% (n>420) and 99% (n=191) of pachytene spermatocytes from adult or juvenile *Ankrd31*$^{-/-}$ mice, respectively. Beyond asynaptic PARs, various abnormal sex chromosome configurations were observed in *Ankrd31*$^{-/-}$ spermatocytes (Figure 3F). This indicates that ANKRD31 plays a more important role in ensuring recombination between the PARs of heterologous sex chromosomes than autosomes.

Delayed formation and resolution of early recombination intermediates in *Ankrd31*$^{-/-}$ meiocytes

To examine the possible reasons that underpin deficiencies in synapsis formation in *Ankrd31*$^{-/-}$ meiocytes we monitored kinetics of recombination intermediates (Figure 4 and S5C). Single-stranded DNA ends resulting from DSBs are marked by recombinases RAD51 and DMC1 and the RPA complex (Hunter, 2015). Levels of these markers on DSB repair intermediates change as recombination progresses. Whereas RAD51 and DMC1 tend to mark intermediates in unsynapsed regions (prevalent in leptotene and early zygotene), RPA accumulates to higher levels on intermediates in synapsed regions (prevalent in late zygotene and early pachytene). Focus numbers of all three markers drop as wild type meiocytes progress to late pachytene, indicating completion of DSB repair at this stage. RAD51, DMC1 and RPA foci accumulated with a delay in *Ankrd31*$^{-/-}$ spermatocytes (Figure 4A-E and S5C). Focus numbers remained abnormally low until early zygotene, increasing only after chromosome axes fully formed (late zygotene-like stage). Thereafter, RAD51, DMC1 and RPA foci persisted in abnormally high numbers until late prophase in *Ankrd31*$^{-/-}$ spermatocytes indicative of a DSB repair defect (Figure 4C-E). To assess kinetics of DSB formation and repair we also measured another DSB marker, serine 139-phosphorylated histone H2AX (γH2AX) (Figure 4F and 4G). γH2AX accumulation is thought to mainly reflect DSB-dependent ATM activity in early prophase, and DSB- and unsynapsed axes-dependent ATR activity after mid zygotene (Barchi et al., 2008; Bellani et al., 2005; Royo et al., 2013). γH2AX levels were much lower in *Ankrd31*$^{-/-}$ than wild type spermatocytes in leptotene and early zygotene, which could indicate a delay in DSB formation or reduced ATM activation in response to DSB formation. The analysis of the pre-DSB recombinosome presented below supports the interpretation of a DSB formation delay. In contrast, γH2AX robustly accumulated on unsynapsed chromatin from late zygotene, consistent with proficient ATR activation on unsynapsed chromatin. This also manifested in the apparently normal accumulation of γH2AX in the unsynapsed chromatin of sex chromosomes, called the sex body, in pachytene (Figure S5D). We also noted that higher numbers of γH2AX flares persisted on synapsed chromatin in late pachytene and diplotene spermatocytes in *Ankrd31*$^{-/-}$ mice as compared to wild-type (Figure S5D and S5E). These γH2AX flares are distinct from the sex body and likely indicate persisting recombination intermediates along synapsed sections of autosomes (Chicheportiche et al., 2007).

ANKRD31 had a qualitatively similar effect on the dynamics of DSB repair proteins in oocytes as compared to spermatocytes (Figure S5F-O). Accumulation of RAD51, DMC1 and RPA foci was delayed, and both RPA and γH2AX signal persisted longer in late prophase in *Ankrd31*$^{-/-}$ oocytes as compared to wild-type.

Overall, our data suggest that accumulation of DSB recombination intermediates is delayed in both sexes of *Ankrd31*$^{-/-}$ meiocytes, which delays and/or compromises SC formation. Persistence of recombination foci also indicates defective and/or delayed DSB repair. These defects provide a plausible explanation for elevated apoptosis in pachytene spermatocytes and oocytes of newborn mice. The DSB repair and SC defects appear subtle enough to allow the production of a cohort of oocytes for reproduction, which however cannot maintain high fertility with increasing age. Likewise, the subtlety of the DSB repair defects could explain the survival of a significant cohort of *Ankrd31*$^{-/-}$ spermatocytes beyond prophase.

COs are lost from PAR in *Ankrd31*$^{-/-}$ spermatocytes

A penetrant defect in the PAR synapsis in spermatocytes (see Figure 3F) prompted us to test if a CO formation defect in X and Y PAR could account for the unaligned chromosomes in metaphase arrested *Ankrd31*$^{-/-}$ spermatocytes (Figure 3B). Hence, we examined if *Ankrd31*$^{-/-}$ spermatocytes are defective in the formation of MLH1 marked recombination foci, which are thought to be precursors of most COs in mid and late pachytene (Figure 5A and 5B, Hunter, 2015). Whereas MLH1 foci formed on autosomes in normal numbers in most *Ankrd31*$^{-/-}$ spermatocytes, MLH1 foci were always absent from the PARs of sex chromosomes in pachytene cells. We also examined chromosome spreads of metaphase spermatocytes. While in wild-type chiasmata were present between each pair of homologs and between sex chromosomes (n=79 cells), no *Ankrd31*$^{-/-}$ spermatocytes had chiasma between X and Y chromosomes as detected by FISH (n=57 cells, Figure 5C). A small fraction of cells (10.12% of 89 cells examined without FISH) also lacked chiasma between an autosome pair. Overall, these observations suggest that MLH1 foci form and mature with high efficiency on autosomes, but never in PARs, in spermatocytes. The loss of PAR-associated COs explains the observed metaphase arrest phenotype of *Ankrd31*$^{-/-}$ spermatocytes. Hence, it is likely that loss of ANKRD31 affects fertility more in males than females because ANKRD31 is required for recombination between male-specific heterologous sex chromosomes.

CO formation may fail in PARs due to an absence of DSBs or a repair defect of existing DSBs. To test these possibilities we detected DSB foci (RPA) in combination with a FISH probe that recognizes PAR sequences that border the heterologous parts of X and Y chromosomes (Figure 5D). RPA foci were present on at least one of the two PARs in most wild type spermatocytes (91.7%, n=169) but only in a minority of (20.9%, n=67) *Ankrd31*$^{-/-}$ spermatocytes in late zygotene or early pachytene. This observation contrasts globally normal RPA focus numbers in *Ankrd31*$^{-/-}$ spermatocytes in late zygotene and early pachytene (Figure 4E). Thus, ANKRD31 seems to be more critical for DSB formation in PARs than in the rest of the genome.

ANKRD31 is required for the normal spatial distribution of meiotic DSBs

The disproportionately severe reduction of DSB repair focus numbers in PARs as compared to autosomes suggested that the spatial distribution of DSB formation is altered in the absence of ANKRD31. To test this possibility we performed genome-wide mapping of single-stranded DNA ends that result from DSB formation in testes of adult mice. We carried out chromatin-immunoprecipitation of the meiosis-specific recombinase, DMC1, and analyzed the immunoprecipitates by sequencing (ssDNA ChIP-seq, SSDS) (Khil et al., 2012; Smagulova et al., 2011) (Figure 6, S6 and Table S6, S7). SSDS informs on the relative steady state levels and genomic distribution of DMC1-associated single-stranded DNA in early recombination intermediates, which are a function of both DSB formation and the half-life of early recombination intermediates.

An increased usage of default hotspots

DSB hotspot numbers were higher in *Ankrd31*$^{-/-}$ (22215) than wild type control (13507) testes as measured by SSDS. We also observed major differences in the spatial distribution of DSB hotspots between *Ankrd31*$^{-/-}$ testis and wild-type (Figure 6A, 6B and S6A). In *Ankrd31*$^{-/-}$ mice, 61% of DSB hotspots overlapped with PRDM9-dependent hotspots of B6 *Ankrd31*$^{+/+}$ (hereafter called B6 hotspots), and 33% overlapped with DSB hotspots of *Prdm9*$^{-/-}$ mice (default hotspots) that mostly associate with active promoters (Brick et al., 2012). A further 6% of the *Ankrd31*$^{-/-}$ hotspots were at previously undescribed sites (hereafter called “new”). In *Ankrd31*$^{-/-}$, the average strength of hotspots overlapping with B6 hotspots was the highest and “new” hotspots were the weakest (Figure 6C).

In addition, a redistribution of the intensity of SSDS signals was observed at hotspots overlapping with B6 hotspots in *Ankrd31*$^{-/-}$ testes. This was illustrated by a lower correlation in hotspot-associated SSDS signals (r=0.76, Pearson) between *Ankrd31*$^{-/-}$ and wild-type than between two wild type samples (r= 0.98) (Figure 6D and 6E). Consistent with an apparent redistribution of single–stranded DNA signal, not all the B6 hotspots were detected as hotspots in *Ankrd31*$^{-/-}$ testes. Weak B6 hotspots were detected in lower proportions in *Ankrd31*$^{-/-}$ testes than strong B6 hotspots (Figure S6B). Likewise, strong default hotspots of *Prdm9*$^{-/-}$ mice emerged as hotspots in *Ankrd31*$^{-/-}$ mice with higher frequency than weak default hotspots (Figure S6C). The combination of these observations suggested that there was a general shift from the use of PRDM9-dependent B6 hotspots towards default hotspots in *Ankrd31*$^{-/-}$ mice. We conclude that there is a differential hotspot usage, and possibly differential DMC1 loading or ssDNA

turnover at hotspots, in *Ankrd31*$^{-/-}$ compared to wild type, which could be influenced by altered timing of recombination initiation.

A strong reduction of DSB activity in the PAR

Given that loss of ANKRD31 altered the distribution of SSDS signal at the hotspot level, we wondered if ANKRD31 may also have differential effects in specific chromosomes and in the PAR. Wild-type to *Ankrd31*$^{-/-}$ SSDS signal ratios were close to one (from 0.96 to 1.11) on each autosome and sex chromosome regions excluding the PAR. In contrast, wild-type to *Ankrd31*$^{-/-}$ ratios were high in the PAR (9.4) and at hotspots within a 150 kb region upstream of X PAR (Figure 6F, 6G and Table S7 see also STAR Methods for mapping reads to PAR). These observations indicate a strong decrease of DSB activity in, and around, the PAR relative to genome average in *Ankrd31*$^{-/-}$ male mice, which supports the hypothesis that ANKRD31 has a particularly critical role in recombination and DSB formation in the PAR.

Histone H3K4me3 distribution on chromatin is similar in wild type and *Ankrd31*$^{-/-}$ testes

Global changes in the timing and the spatial distribution of DSBs in *Ankrd31*$^{-/-}$ mice could be caused by a change in the testicular transcriptome or altered chromatin organisation. However, we detected very few, if any, changes in the testis transcriptome of juvenile (12 days old) *Ankrd31*$^{-/-}$ mice relative to wild-type (Figure S6D and S6E). Testicular PRDM9 protein levels were also similar in *Ankrd31*$^{-/-}$ and wild type testes (Figure S6F). Both PRDM9-dependent and PRDM9-independent hotspots are characterized by enrichment for histone H3K4me3, therefore we performed histone H3K4me3 ChIP-seq on testes of juvenile mice (12 days old) to test if an altered distribution of H3K4me3 could explain the patterns of DSB formation in *Ankrd31*$^{-/-}$ mice (Figure 6A and 6G). To allow better comparison of different samples we normalized H3K4me3 signal to a common set of transcription start sites (Davies et al., 2016 and STAR Methods).

H3K4me3 signal enrichment appeared highly similar in wild type and *Ankrd31*$^{-/-}$ mice both at B6 hotspots and PRDM9-independent hotspots including the broader region of the PAR (Figure 6A, 6G, and Table S7). Indeed, histone H3K4me3 enrichment strongly correlated between wild type and *Ankrd31*$^{-/-}$ testes at B6 (r=0.99) and default (r=0.99) hotspot sites (Figure 6H, 6I) indicating that PRDM9-dependent and -independent H3K4me3 depositions are not affected in *Ankrd31*$^{-/-}$ mice. Furthermore, we found no significant correlation between the variation of wild-type to *Ankrd31*$^{-/-}$ SSDS signal ratios and H3K4me3 signal ratios at B6 hotspots (Figure S6G).

Together, these observations suggest that ANKRD31 is required for neither PRDM9 methyltransferase activity at B6 hotspots nor the accumulation of H3K4me3 at PRDM9-

independent hotspots including the PAR. The shift in DSB activity from B6 to default hotspots and the severe reduction of DSB activity in the PAR in *Ankrd31*$^{-/-}$ mice are therefore not due to changes in histone H3K4me3 levels.

Timely assembly of DSB-promoting proteins into chromatin-bound complexes depends on ANKRD31

Given its localization on axes, ANKRD31 might modulate the function of pre-DSB recombinosomes, which could provide a feasible explanation for *Ankrd31*$^{-/-}$ phenotypes. Consistent with this hypothesis we found that both MEI4 and REC114 foci appeared with delayed kinetics in *Ankrd31*$^{-/-}$ spermatocytes (Figure 7A-C and S7A-C). Nevertheless, MEI4 and REC114 foci did accumulate by zygotene and persisted until SC formation was complete. Kinetics of MEI4 and REC114 focus formation matched those of early recombination intermediates (RAD51, DMC1 and RPA foci), suggesting that a delay in the formation of MEI4- and REC114-marked pre-DSB recombinosomes contributes to a delay in DSB formation in *Ankrd31*$^{-/-}$ meiocytes.

Robust aggregates of DSB-promoting proteins in PARs depend on ANKRD31

Whereas MEI4 and REC114 foci eventually formed in *Ankrd31*$^{-/-}$ meiocytes, we did not observe MEI4 and REC114 aggregates in PARs or autosome ends (Figure 7B and S7B). We also noticed an alteration of chromosome axis in PARs in *Ankrd31*$^{-/-}$ meiocytes. SYCP3-staining appeared brighter and/or thicker at the PAR-end of sex chromosomes (particularly on Y chromosome) in late zygotene and at the zygotene-to-pachytene transition in wild-type (Figure 1F, 7D and S7D, Page et al., 2012). This alteration of PAR axes was also highlighted by a marked enrichment of IHO1, which is both a component of pre DSB-recombinosomes and a recombinosome-independent marker of unsynapsed axes (Stanzione et al., 2016). Thus, while IHO1 was not required for MEI4, REC114 and ANKRD31 aggregates (Figure 2J, S3H and S3I), IHO1 accumulation paralleled formation of MEI4 and REC114 aggregates (Figure 2G and S3C), and also persisted in PARs after synapsis initiation (Figure S7D and S7E).

In *Ankrd31*$^{-/-}$ spermatocytes, IHO1 robustly decorated unsynapsed axes, but its PAR-enrichment was strongly reduced; only a weak enrichment of IHO1 could be discerned in a small minority of late zygotene and zygotene-to-pachytene transition cells (15.56%, n=59 cells, n=2 mice). Mirroring this change, the bright/thickened SYCP3 stain was abolished in PARs in *Ankrd31*$^{-/-}$ spermatocytes. Together, these observations suggest that ANKRD31 is required for the establishment of a specialized PAR axis domain that is particularly rich in DSB-promoting proteins.

Discussion

We identify ANKRD31 as a key meiotic protein that regulates spatial and temporal patterns of pre-DSB recombinosome assembly and recombination activity in mice. Our findings are supported by similar observations of Boekhout et al. 2018 and Acquaviva et al. 2019.

ANKRD31 is part of the pre-DSB recombinosome

ANKRD31 colocalizes with highly conserved protein components of pre-DSB recombinosomes (Figure 2, S3) (IHO1, MEI4 and REC114 in mice) (de Massy, 2013; Kumar et al., 2010; Kumar et al., 2018; Stanzione et al., 2016). Although the precise architecture of these complexes is unknown, ANKRD31 association with pre-DSB recombinosomes seems to involve direct interactions with REC114 and IHO1 (Figure 2, S3 and Boekhout et al. 2018). We observed two types of pre-DSB recombinosomes, foci and aggregates. Foci formed genome-wide (Kumar et al., 2010; Stanzione et al., 2016), aggregates formed in PARs and at the distal ends of chromosome 4, 9 and 13, which share homology with PAR as identified by Acquaviva et al. 2019, and reconfirmed by us using FISH (unpublished data). We refer to these autosomal sites as PAR-like regions. Pre-DSB recombinosome foci and aggregates have distinct properties. Focus formation requires IHO1 and is enhanced by, but not dependent on, ANKRD31. In contrast, aggregate formation is independent of IHO1 but requires ANKRD31. IHO1 is thought to recruit pre-DSB recombinosomes to axes in most of the genome through its interaction with HORMAD1. Hence, we propose that the mode of pre-DSB recombinosome recruitment to axes is altered in PARs and PAR-like regions. MEI4, REC114 and ANKRD31 are mutually dependent for aggregate formation (Figure S3), and ANKRD31 might be a specificity-factor that recognizes some properties of PARs and PAR-like regions to allow aggregates. Alternatively, ANKRD31 might confer specific properties on pre-DSB recombinosome components, enabling them to be enriched in the unique chromatin environment of PAR and PAR-like regions. ANKRD31 also impacts on the organisation of chromosome axes, as a noticeable thickening of axes in PARs depends on ANKRD31 (Figure 7D). The formation of a disproportionately long PAR axis, short DNA loops and extensive axis splitting, which underlies the axis thickening in our study, all depend on ANKRD31 (Acquaviva et al., 2019). Whether ANKRD31 reorganizes PAR chromatin directly or indirectly (via MEI4 or REC114) is unknown.

ANKRD31 may control recombination initiation by regulating pre-DSB recombinosomes

Beyond altered pre-DSB recombinosome formation, our study revealed two clear consequences of ANKRD31 deficiency for recombination initiation. First, a delay in DSB repair focus formation and, second, a change in the localization and relative levels of DSBs along chromosomes as

459 measured by SSDS, with the most noticeable consequences in the PAR. The delay in the
460 accumulation of early recombination intermediates (DMC1, RAD51 and RPA foci) matched the
461 delayed appearance of pre-DSB recombinosome foci in *Ankrd31*$^{-/-}$ spermatocytes. We thus
462 propose that ANKRD31 enhances pre-DSB recombinosome focus assembly, which helps timely
463 initiation of recombination and SC formation between homologs (Figure S7E). A related, but
464 possibly distinct, molecular function of ANKRD31 may permit aggregate formation of DSB-
465 promoting proteins in PARs, thereby ensuring obligate recombination initiation in this region
466 (Figure S7E).

467

468 **Altered DSB localization to PRDM9-independent sites in *Ankrd31*$^{-/-}$ mice.**

469 DSB activity at PRDM9-independent default sites is normally repressed in wild-type by a poorly
470 understood PRDM9-dependent mechanism, which may reflect competition between PRDM9-
471 dependent and independent sites (Brick et al., 2012; Diagouraga et al., 2018). This control
472 seems important, because extensive DSB activity at default sites is thought to cause asynapsis
473 and delay in DSB repair (Brick et al., 2012; Hayashi et al., 2005). One of the striking features of
474 the change in DSB localization in *Ankrd31*$^{-/-}$ mice is the use of default sites, which could
475 contribute to the synapsis defect and delayed DSB repair kinetics in *Ankrd31*$^{-/-}$ mice. It is unlikely
476 that use of default sites is due to changed PRDM9 activity in *Ankrd31*$^{-/-}$ meiocytes, since histone
477 H3K4me3 distribution was not significantly changed (Figure 6, S6 and Table S7). We favor the
478 idea that default site usage is a consequence of altered pre-DSB recombinosome regulation.
479 ANKRD31-dependent properties of pre-DSB recombinosome could impact upon competition
480 between PRDM9-dependent and independent sites. Alternatively delayed DSB formation might
481 by itself promote the usage of default sites in *Ankrd31*$^{-/-}$ mice. A potential link between timing of
482 DSB formation and usage of PRDM9-independent sites has been previously observed; PAR-
483 associated DSBs are mostly independent of PRDM9 and form later than autosome-DSBs
484 (Kauppi et al., 2011).

485

486 **DSB control on the PAR**

487 The PAR region is highly enriched for DSBs compared to the genome average (Kauppi et al.,
488 2011; Lange et al., 2016), and we found that this enrichment requires ANKRD31 (Figure 6 and
489 Table S7). Intriguingly, DSBs were lost from the PAR in *Ankrd31*$^{-/-}$ mice independently of histone
490 H3K4me3 enrichment (Figure 6 and Table S7). Enrichment of histone H3K4me3 had previously

been linked to high DSB activity in the PAR (Brick et al., 2012) but is not sufficient to ensure high DSB numbers according to our results. We propose that robust DSB formation in the PAR requires an ANKRD31-dependent enrichment of pre-DSB recombinosomes (Figure 7 and S7) and/or ANKRD31-dependent alterations to axis/loop organisation as also suggested by (Acquaviva et al., 2019; Kauppi et al., 2011). Thus, the distribution of pre-DSB recombinosomes on axes seems to have a crucial role in defining genomic sites where DSBs occur.

Curiously, for unknown reasons, DSB activity is PRDM9-independent in the PAR in mice (Brick et al., 2012). We speculate that this might have arisen due to the erosion of PRDM9-binding sites during evolution. Such erosion occurs when the template used for the repair of DSBs at hotspots includes polymorphisms that disrupt PRDM9 binding sites (Lesecque et al., 2014; Myers et al., 2010). Since the strength of this effect increases with hotspot strength, high DSB activity in the PAR region is expected to erode PRDM9 sequence motifs faster than in other genomic regions. One way in which species could cope with the loss of PRDM9 binding sites is the concurrent evolution of the PRDM9 protein (Latrille et al., 2017). Another way is to use localized PRDM9-independent DSB initiation, which might require relieving PRDM9-dependent repression of default hotspot sites in this region, without affecting PRDM9 control in the rest of the genome. This could occur by delaying DSB formation in the PAR to a time-window where PRDM9 is inefficient in providing competitive advantage to PRDM9-dependent hotspot sites and/or blocking default hotspots. A non-exclusive mechanism could be the assembly of pre-DSB recombinosome aggregates with unique characteristics, which might permit the establishment of a PAR-specific chromatin environment where PRDM9-independent DSBs are possible. PRDM9-independent formation of DSBs in the PAR is not a universal feature, since there are PRDM9-dependent hotspots in human PARs (Pratto et al., 2014; Sarbajna et al., 2012). It will be interesting to determine whether the high level of accumulation of pre-DSB proteins is an evolutionary conserved feature of PARs, or if it is linked to PRDM9-independence in DSB formation. We predict that high accumulation of pre-DSB recombinosome proteins will promote high DSB density, regardless of the extent of PRDM9 involvement.

Conclusions

The behavior of ANKRD31 and the phenotype of *Ankrd31*$^{-/-}$ meiocytes show that correct timing and spatial patterning of recombination initiation are dependent on ANKRD31 in mice. Our observations strongly suggest that ANKRD31 performs these functions by modulating the properties, formation kinetics and/or the stability of complexes of essential DSB-promoting

proteins localized on chromosome axes. The phenotype of *Ankrd31*$^{-/-}$ mice provides support for the previously untested hypothesis that spatial patterning of recombination initiation is controlled not only by the chromatin environment of potential DSB sites in chromatin loops, but also by the DSB forming machinery that assembles in the topologically distinct compartment of the chromosome axis. This paradigm is best exemplified in the PARs of heterologous sex chromosomes, where obligate recombination seems to depend on ANKRD31-mediated enrichment of DSB promoting proteins and modification of chromatin organisation.

ACKNOWLEDGEMENTS

We thank L. Acquaviva, M. Boekhout, M.E. Karasu, M. Jasin and S. Keeney for sharing critical unpublished results; D. Tränkner and M. Munzig for lab support, R. Jessberger for departmental support and sharing ideas and reagents (anti-SYCP3); M. Stevense, G. Pearce and E. Hoffmann for editing and proofreading the manuscript; Transgenic Core of MPI-CBG for CRISPR injections; Experimental Center of MTZ for antibody production and mouse husbandry; BIOTEC Deep Sequencing for RNA-sequencing and bioinformatics support; the MPI-CBG scientific computing facility for last minute bioinformatics support; I MacGregor, A.M Pendes, L.G. Hernandez for testing ANKRD31 antibodies in various mammalian species; K. Daniel for ovarian and testicular RNA preparation; Christine Brun for immune-cytochemistry support; Montpellier Resources Imagerie (MRI) for microscopy, the ENCODE Consortium and the ENCODE production laboratory(s) for mouse tissue transcriptome datasets. The Deutsche Forschungsgemeinschaft (DFG; grants: TO421/3-1/2, TO421/6-1/2, TO421/7-1, TO421/10-1, TO421/5-1, TO421/8-1/2) and HFSP research grant RGP0008/2015 supported F.P., I.D., R.R., S.V. and A.T. DIGS-BB Program supported A.B. J.C.. C.G. and B.d.M. were funded by grants from the Centre National pour la Recherche Scientifique (CNRS) and the European Research Council (ERC) Executive Agency under the European Community's Seventh Framework Programme (FP7/2007-2013 Grant Agreement no. [322788]). B.d.M. was recipient of the Prize Coups d'Élan for French Research from the Fondation Bettencourt-Schueller. E.T. and M.B. were funded by Telethon Foundation, (Grant GGP12189) and Mission Sustainability Grant, University of Rome Tor Vergata (Grant 141). D.L., P.J. and J.F. were funded by Czech Science Fundation (CSF): grant 13-08078S to J.F. Ministry of Education, Youth and Sports (MEYS): LQ project of the NSPII to J.F. Boehringer Ingelheim GmbH and Austrian Academy of Sciences supported A.S. Medical Research Council grant number MC_UU_00007/6 supported I.R.A.

AUTHOR CONTRIBUTIONS

F.P. generated ANKRD31 antibodies and *Ankrd31*$^{-/-}$ mice, characterized *Ankrd31*$^{-/-}$ male phenotype

J.C., ChIP-seq bioinformatics

E.T., PAR-FISH

I.D. assisted characterization of *Ankrd31*$^{-/-}$ male phenotype, performed ANKRD31 colocalization experiments, analyzed PAR-FISH experiments and ANKRD31 localization in *Mei4*$^{-/-}$ mice, and produced H1t antibody

R.R., *Ankrd31*$^{-/-}$ female analysis

C.G. performed ChIPs, constructed libraries, purified PRDM9 antibody and measured PRDM9 protein levels in *Ankrd31*$^{-/-}$

A.B.,Y2Hs and immunoprecipitation-WB of ANKRD31

S.V.C. validated ANKRD31 antibodies, analysed ANKRD31 localization and apoptosis in testis cryosections

A.S., multiple alignments of ANKRD31 sequences

M.S., initial Y2Hs and initial IHO1 localization analysis in PAR

P.J., D.L. and J.F., chromosome FISH

F.J., CRISPR/CAS9 mRNA and gRNA preparation

I.R.A., provided fetal ovaries for screening, and copy-edited manuscript

M.B. analyzed PAR-FISH experiments, supervised E.T. and revised the manuscript

B.d.M. performed ANKRD31 localization experiments in *Mei4*$^{-/-}$ and *Rec114*$^{-/-}$ mice, analyzed data and co-wrote the section on ChIP-seq, introduction and discussion with A.T. and revised the manuscript.

A.T. designed experiments, analyzed data, supervised the project and wrote the manuscript with input from other authors.

Declaration of Interests

The authors declare no conflict of interest.

Figure Legends

Figure 1. ANKRD31 is a meiotic protein that preferentially localizes to unsynapsed axes

(A-B) *Ankrd31* transcript levels are shown as transcripts per million (TPM) in (**A**) total RNAs of fetal ovaries at the indicated developmental stages, or (**B**) mixtures of equal quantities of total RNAs of 17 somatic tissues (somatic) or 17 somatic tissues plus adult testes (testis+ somatic). (**C**) DNA staining by DAPI and immunostaining of ANKRD31 and a meiotic chromosome axis marker, SYCP3, in testis sections. Guinea pig antibodies against an N-terminal fragment of ANKRD31 (Gu-ANKRD31 Nt) were used. Seminiferous tubules at stage IX and X are shown; see STAR Methods for staging. Sertoli cells (se), leptotene (le), zygotene (zy), late pachytene (lpa), and diplotene (di) spermatocytes and elongating spermatids (es) are marked. Gu-ANKRD31 Nt antibodies stained some interstitial cells strongly (yellow arrowhead), and Sertoli cell nuclei weakly. We consider these signals non-specific as they were not reproduced by rabbit antibodies against the same ANKRD31 fragment (Rb-ANKRD31 Nt), see Figure S1B. (**D-F)** ANKRD31, SYCP3 and a marker of synapsis, SYCP1 (transverse filament protein), were stained in spread spermatocytes of adult mice. Rb-ANKRD31 Nt antibodies stained ANKRD31. Matched exposed images of ANKRD31 are shown. SYCP3 and SYCP1 were differentially levelled to optimize viewing of overlay images. Insets of late zygotene and zygotene-pachytene spermatocytes are enlarged in **E** and **F**, respectively. X and Y chromosomes and unsynapsed (unsy) and synapsed (sy) regions of an autosome are marked in some images of **D-F**. In **F**, arrowhead and arrow mark a large and a small aggregate of ANKRD31 on the PAR ends of sex chromosomes and the end of an autosome, respectively. Bars, 50µm (**C**), 10µm (**D**), 2.5µm (**E, F**). (**G**) ANKRD31 focus counts (Rb-ANKRD31 Nt) in preleptotene (prele), leptotene (le), early zygotene (ezy) and late zygotene (lzy) spermatocytes. Cell numbers (n) and medians (bars) are shown. See also Figure S1, S2 and Table S1.

Figure 2. ANKRD31 colocalizes with DSB-promoting proteins on chromosome axes, and forms aggregates in PARs and PAR-like regions

(**A, D, G, J**) Immunostained spermatocyte spreads. MEI4 (**A**) and REC114 (**D**) signals are shifted to the right by three pixels in the enlarged insets. Arrowheads mark co-aggregates of ANKRD31, MEI4 and REC114. (**B, C, E, F**) Quantification of overlap between ANKRD31 and MEI4 (**B, C**) or REC114 (**E, F**) foci in leptotene (le) and early zygotene (ezy) spermatocytes. Overlap was significantly reduced when ANKRD31 images were turned 90 degree (turn, red) relative to MEI4 or REC114 images, Wilcoxon signed rank test, $P<0.0001$,(****). (**G, left panel**) Arrowheads mark co-aggregates of ANKRD31 and MEI4 in the PAR and at three autosome ends in a spermatocyte at zygotene-to-pachytene transition. (**G, right panel**) Arrow marks PAR in enlarged insets. (**H**) Schematics of ANKRD31 domains and Y2H interactions. Colored boxes mark ankyrin repeats (ANK1 and ANK2), coiled coil domain (CC), and conserved regions 4

(CR4) and 5 (CR5). Blue lines and numbers show ANKRD31 residues that interact with the indicated proteins in Y2H. + and ++ mark weak and strong interactions, respectively. (**I**) ANKRD31 focus counts in preleptotene (prele), leptotene (le), early (ezy) and late (lzy) zygotene spermatocytes. Cell numbers (n) and medians (bars) are shown. Mann–Whitney U test, 0.001<P<0.05 (**) and P<0.0001 (****). (**J**) *Iho1*$^{-/-}$ spermatocyte with fully formed chromosome axes. Enlarged insets (bottom panel) show a co-aggregate of ANKRD31 and REC114. (**A**, **D**, **G** and **J**) Bars, 10µm in low resolution images and 5µm in enlargements. See also Figure S3, Table S2 and S3.

Figure 3. SC formation is defective in *Ankrd31*$^{-/-}$ spermatocytes

(**A**) Targeting of *Ankrd31* exon 6 by CRISPR/Cas9. Sequences of guide RNA (gRNA, PAM (underlined) and exon 6 (capital)/intron6 (lower case) boundaries are shown in wild-type (WT) and mutant lines (mut1 and 2). (**B**) DAPI staining of DNA in testis sections. Seminiferous tubules with metaphase spermatocytes are shown (stages XII in wild–type, XII-like in *Ankrd31*$^{-/-}$, see STAR Methods). Sertoli cells (se), zygotene spermatocytes (zy), metaphase cells (m), lagging chromosomes (la) and immature sperm (sp) are marked. The middle panel shows enlarged colour-coded insets. Bars, 50µm (sections) and 5µm (zoom). (**C**) Quantification of seminiferous tubules that contain metaphase spermatocytes. Number of tubules (n) counted in four experiments, weighted averages of percentages and standard deviation are shown. (**D-F**) SC (SYCP1) was detected in combination with axis marker (SYCP3) in *Ankrd31*$^{+/+}$ and *Ankrd31*$^{-/-}$ spermatocytes. (**D**) Indicated categories of SYCP1 staining patterns were quantified in populations of histone H1t-negative spermatocytes that had short axis (equivalent to wild type leptotene), long incomplete axes (early zygotene), or fully formed continuous axes (late zygotene and early pachytene cells). Spermatocytes of adults or 13 day old juvenile mice were examined. Cell numbers (n), standard deviation and the weighted averages of three (adults) or two (juvenile, 13 days old) experiments are shown. (**E, F**) SYCP3 and SYCP1 stainings in spread spermatocytes. (**E**) Images represent axis development categories of **D**. (**F)** Sex chromosome configurations in wild type and *Ankrd31*$^{-/-}$ spermatocytes. The dominant fraction of *Ankrd31*$^{-/-}$ spermatocytes (76%) has unsynapsed X and Y chromosomes without other apparent abnormalities. Minor fractions have self-synapsed or short Y axes (12.5%), X-autosome fusions (6.6%) or circularized Y (4.8%), n=271 spermatocytes. X (arrows) and Y (arrowhead) chromosomes are marked. (**E, F**) Bars, 10µm. (**C, D**) Chi Square test, non-significant (ns) and P<0.0001 (****). See also Figure S4, S5, Table S4, and S5.

Figure 4. Delayed kinetics of recombination foci in *Ankrd31*$^{-/-}$ spermatocytes

(**A, B, F**) Immunostained spermatocyte spreads. Bars, 10µm. Early zygotene cells are shown in **A** and **B**. DMC1 (**C**), RAD51 (**D**), and RPA (**E**) focus numbers and total nuclear γH2AX signal (**G**) are shown in spermatocytes at stages (**C, D, E**) leptotene (le), early zygotene (ezy), late zygotene (lzy), early pachytene (epa), mid pachytene (mpa) and late pachytene (lpa), (**G**) pooled leptotene and early zygotene (le-ezy) or late zygotene (lzy). (**C, D, E, G**) Cell numbers (n) and medians (bars).are shown. Mann–Whitney U test, non-significant P>0.05 (ns), P>0.01 (*), P>0.001 (**) and P<0.0001 (****). See also Figure S5.

Figure 5. PARs fail to engage in *Ankrd31*$^{-/-}$ spermatocytes

(**A**) Immunostaining in spread mid pachytene spermatocytes, as identified by histone H1t staining (miniaturized H1t stain in, the corner of overlay images). Arrowheads mark MLH1 focus in PAR in enlarged images of X and Y chromosomes. (**B**) MLH1 focus numbers in mid-to-late pachytene. Cell numbers (n) and medians (bars) are shown. Mann–Whitney U test, 0.01>P>0.001 (**). (**C**) FISH stained X and Y chromosomes in metaphase spreads; DAPI stained DNA. (**D**) PAR FISH combined with SYCP3 and RPA staining in spread spermatocytes. One late zygotene *Ankrd31*$^{+/+}$ and two early pachytene *Ankrd3*$^{-/-}$ are shown. Enlargements of boxes are below respective full nucleus images. White dashed lines mark boundaries between PAR FISH signals and the rest of chromosome X or Y. Arrowheads mark axis-associated RPA foci within or distal to PAR signals. Y chromosome PAR images are enlarged from both *Ankrd31*$^{-/-}$ cells (Y_1 and Y_2). Enlarged image of X chromosome PAR is only shown from one of the cells (X_1), because the X PAR overlays an autosomal axis in the other cell (X_2). Bars, 10µm (**A, C, D**), and 5µm (**A**) or 2.5µm (**D**) in enlargements.

Figure 6. Spatial distribution of DSBs is altered in the absence of ANKRD31

(**A, G**) DMC1 ChIP SSDS and histone H3K4me3 signal coverage (merged from two experiments) are shown in the indicated mouse lines in a 150kb region of chromosome 1 in **A** and in the broader PAR region of X chromosome in **G**. (**A**) Blue and black arrows mark sites of published C57BL/6J (B6) hotspots and PRDM9-independent default hotspots from Diagouraga et al. 2018 and Brick et al. 2012, respectively. Long and short black arrows represent comparatively strong or weak hotspots in *Prdm9*$^{-/-}$ mice according to DMC1 SSDS coverage. (**B**) Proportion of *Ankrd31*$^{-/-}$ hotspots that match PRDM9-defined (i.e. B6) or default hotspots, or that do not match either (new). (**C**) Average plots (top) and heatmaps (bottom) of DMC1 SSDS signal in *Ankrd31*$^{-/-}$ mice at hotspots overlapping with B6, with default (i.e. from *Prdm9*$^{-/-}$) or with neither of those (new). (**D, E**) SSDS signal comparison at PRDM9-defined hotspots between *Ankrd31*$^{+/+}$

and *Ankrd31*$^{-/-}$ in **D**, or between *Ankrd31*$^{+/+}$ and wild-type C57BL/6J mice (data from Diagouraga et al. 2018) in **E**.

(**F**) *Ankrd31*$^{+/+}$ to $^{-/-}$ DMC1 SSDS signal ratios are shown for each autosome, the non-PAR regions of X (X^{np}) and Y (Y^{np}), and available sequence of the X PAR. (**G**) Arrows mark PRDM9-independent hotspots in the non-PAR region upstream of PAR. (**H-J**) Comparisons of normalized H3K4me3 signals at PRDM9-defined (B6) (**H**), default (**I**) or new (**J**) hotspots sites between *Ankrd31*$^{+/+}$ and *Ankrd31*$^{-/-}$ mice. (**D, E, H-J**) Dotted red lines represent one to one relationship between x and y. Levels represent the density calculated with the density2d function from R. Pearson´s correlation coefficient (r) is indicated with significance (p). See also Figure S6, Table S6 and S7.

Figure 7 ANKRD31 is required for timely MEI4 focus formation and the enrichment of DSB-promoting proteins in PARs

(A, B, D) Immunofluorescence of indicated proteins and centromere (CENT) in spread spermatocytes in leptotene (**A**) and late zygotene (**B, D**). (**A, B**) MEI4 exposures were matched between genotypes. (**B**) Arrowheads mark MEI4 aggregates. Fractions of late zygotene spermatocytes with MEI4 aggregates are shown in MEI4 images. (**C**) MEI4 focus numbers in preleptotene (prele), leptotene (le), early (ezy) and late (lzy) zygotene spermatocytes. Cell numbers (n) and medians (bars) are shown. Mann–Whitney U test, 0.01>P>0.001 (**), P<0.0001 (****). (**D**) Boxed X and Y chromosomes are enlarged in bottom panels, arrows mark PAR, arrowheads mark centromeric ends. Bars, 10µm (**A**, **B** and **D)** and 5µm **(D** in enlargement**).** See also Figure S7.

STAR METHODS

CONTACT FOR REAGENT AND RESOURCE SHARING

Further information and request for resources and reagents should be directed to the Lead Contact, Attila Toth (attila.toth@mailbox.tu-dresden.de).

EXPERIMENTAL MODEL AND SUBJECT DETAILS

Animal experiments, choice of adults or juveniles

Gonads were collected from mice after euthanasia. Most cytological experiments of spermatocytes were carried out on samples collected from adult mice unless indicated otherwise. In particular, we used juvenile mice (13-14 days old) to enrich for cells that are in late zygotene or zygotene-to-pachytene transition. Juvenile mice were also used for transcriptome analysis and histone H3K4me3 ChIPseq, where differences between the cellularities of testes in adult wild type and *Ankrd31*$^{-/-}$ mice would have complicated interpretation of experimental outcomes. The first wave of spermatocytes reaches mid pachytene in 14 days old mice, at which point cellularities of testes in wild type and *Ankrd31*$^{-/-}$ mice begin to differ due to apoptosis of spermatogenic cells in the latter. Transcriptomes and histone H3K4me3 patterns are expected to greatly differ in meiotic and non-meiotic cell populations of testes. Therefore, altered relative proportions of these cell populations differentiate transcriptomes and histone H3K4me3 ChiPseq signal distributions in testes of wild-type and *Ankrd31*$^{-/-}$ mice that are older than 13-14days. Hence, we used 12 days old mice for these experiments.

Animals were used and maintained in accordance with the German Animal Welfare legislation ("Tierschutzgesetz"). All procedures pertaining to animal experiments were approved by the Governmental IACUC ("Landesdirektion Sachsen") and overseen by the animal ethics committee of the Technische Universität Dresden. The licence numbers concerned with the present experiments with mice are T 2014-1 and TV A 8/2017.

Generation of *Ankrd31*-knockout mice

Ankrd31 mutant lines were generated using CRIPSR/Cas9 genome editing (Hwang et al., 2013), targeting exon6 of *Ankrd31* gene. A mixture of gRNA: AGTCACCAAAACACTGG (12.5 ng/µl) (designed using the online platform at http://crispr.mit.edu/) and Cas9 nuclease mRNA (50 ng/µl) was injected into pronucleus/cytoplasm of fertilized oocytes. The oocytes were subsequently transferred into pseudopregnant recipients. Injections and embryo transfer were performed by Transgenic Core Facility of MPI-CBG (Dresden, Germany). Out of 115 injected embryos, 82 were transferred into females and 15 were born. 14 of the 15 born pups had alterations in the targeted genomic locus. Two mice that were heterozygote for predicted frame-shift causing alleles (mut1 and mut2, Figure 3A) were bred with C57BL/6JCrl wild type mice to establish mouse lines. All experiments reported in the manuscript are based on samples from mice that were derivative of founder lines after at least three backcrosses.

METHOD DETAILS

CRISPR/Cas9 procedures

gRNA production

The guide RNA **(**gRNA**)** expression vector DR274 (Addgene #42250) was used to construct the gRNA (Hwang et al., 2013). Primers encoding gRNA sequence were annealed to form double-strand DNA with overhangs for ligation into DR274 vector that was linearized with BsaI restriction enzyme (NEB). PCR product was amplified from the resulting plasmid with DR274_F/DR274_R primers and used as a template for *in vitro* transcription with MEGAscript™ T7 Transcription Kit (Ambion).

CAS9 mRNA preparation

To prepare Cas9 mRNA, we first used the restriction enzyme PmeI to linearize the plasmid MLM3613 (Addgene #42251) (Hwang et al., 2013) that harbors a codon optimized Cas9 coding sequence and a T7 promoter for Cas9 mRNA *in vitro* synthesis. We then used the linearized MLM3613 as template to synthesize the 5′ capped and 3′ polyA-tailed Cas9 mRNA using the mMESSAGE mMACHINE® T7 Ultra Kit (ThermoFisher, cat no: AM1345) according to the manufacturer's instructions.

Genotyping *Ankrd31*-knockout mice

Tail biopsies were used to generate genomic DNA by overnight protease K digestion at 55°C in lysis buffer (200mM NaCl, 100mM Tris-HCl pH 8, 5mM EDTA, 0.1% SDS). Following heat inactivation for 10 min at 95°C. These genomic preparations were used for PCR. F0 mice were genotyped by PCR amplification followed by PAGE electrophoresis and DNA sequencing. Mice in subsequent crosses were genotyped by PCR amplification followed by agarose gel electrophoresis. Combination of four primers, AS-79WT-FW2, Ank_ex5gen_LngR, Ank_ex5gen_LngFW, KO79-RV, were used to genotype the *Ankrd31*^{mut1} allele. PCR product sizes were 623bp and 262bp for wild type, and 624bp and 400bp for *Ankrd31*^{mut1} allele. Two primers, Ank_ex5_gen_shFW and Ank_ex5_gen_shR, were used to genotype *Ankrd31*^{mut2} allele. PCR product sizes were 281bp for wild type, and 248bp for *Ankrd31*^{mut2} allele.

Generation of antibodies against fragments of ANKRD31, Histone H1t and REC114

Antibodies were raised against two ANKRD31 fragments (N-terminal fragment, 144 amino acids between Thr182 and Met325 residues, C-terminal fragment, 153 amino acids between Pro1470 and Arg1622 residues), full length Histone H1t, and two REC114 fragments (N-terminal, 130 amino acids between Met1 and Glu130 residues, C-terminal fragment, 129 amino acids between Arg131 and Asn259 residues). Coding sequences corresponding to these peptides were cloned into pDEST17 bacterial expression vector. Recombinant 6xHis-tagged proteins were expressed in *E. coli* strain, BL21 tRNA (ANKRD31) or BL21(DE3)pLysS (Histone H1t and REC114) , and

subsequently purified on Ni-Sepharose beads (Cat. no. 17-5318-01, Amersham, GE Healthcare). Purified proteins were used for immunization of rabbits and guinea pigs. ANKRD31 fragments coupled to NHS-Activated Sepharose 4 Fast Flow beads (Cat. no. 17-0906-01, Amersham, GE Healthcare) were used to affinity purify polyclonal antibodies following standard procedures.

ANKRD31 immunoprecipitation and western blotting

For preparation of protein extracts from wild type and *Ankrd31*-deficient testes, testes of 12 days old juvenile mice were detunicated and homogenized in a lysis buffer (50 mM Tris-HCl pH 7.5, 150 mM NaCl, 0.5% Triton X-100, 1 mM $MgCl_2$). Lysis buffer was supplemented with protease inhibitors and phosphatase inhibitors: 1 mM Phenylmethylsulfonyl Fluoride (PMSF); complete™ EDTA-free Protease Inhibitor Cocktail tablets (Roche, 11873580001); 0.5 mM Sodium orthovanadate; Phosphatase inhibitor cocktail 1 (Sigma, P2850) and Phosphatase inhibitor cocktail 2 (Sigma, P5726) were used at concentrations recommended by the manufacturers. Testis homogenates were lysed for 60 min at 4˚C in the presence of benzonase (Merck Millipore) to digest DNA during lysis. Lysates were spun at 1000 g for 10 min. Supernatants were diluted two times with 50 mM Tris-HCl pH 7.5, 150 mM NaCl, mixed with 1 µg of rabbit anti-ANRKD31 C-terminal antibody and incubated for 2.5 h at 4˚C. 1.5 mg of Dynabeads™ Protein A (Invitrogen) were added to the lysate-antibody mix and incubated for 4 h at 4˚C. Beads were washed twice with washing buffer (50 mM Tris-HCl pH 7.2, 150 mM NaCl, 0.25% Triton X-100). Immunoprecipitated material was eluted from the beads by incubating the beads in 100 µl Laemmli sample buffer for 10 min at 70˚C. The proteins from resulting elutions and input samples were separated on 4-15% TBX-acrylamide gradient gel (Bio-Rad) and blotted onto PVDF membrane (Sigma, P2938). Membranes were blocked for 1 h at room temperature using blocking solution (5% skimmed milk, 0.05% Tween 20, in TBS pH 7.6) and incubated overnight at 4°C with guinea pig anti-ANKRD31 N-terminal (1:1000) and mouse anti-GAPDH (1:1000) primary antibodies diluted in 0.05% Tween 20 in TBS pH 7.6 (TBS-T). Afterwards, horseradish peroxidase (HRP)-conjugated secondary antibodies (diluted in 2.5% skimmed milk in TBS-T) were applied for 1 h at room temperature. Detection of secondary antibodies was performed with Immobilon Western Chemiluminescent HRP Substrate (Millipore).

Cytoplasmic and nuclear fractionation for PRDM9 detection

Juvenile mouse testes were homogenized in hypotonic buffer (10 mM Hepes, pH 8.0, 320 mM sucrose, 1 mM PMSF, 1x Complete protease inhibitor cocktail EDTA-free (Roche, Cat. Number 11873580001)) and phosphatase inhibitor 1x (Thermo Scientific, Halt Phosphatase Inhibitor Cocktail, Cat Number 78420) in a glass douncer. Testis cell suspensions were centrifuged at

1000g at 4°C for 10 min. Supernatants were collected and used as cytoplasmic fractions. Pellets were resuspended in RIPA buffer (50 mM Tris-HCl, pH 7.5, 150 mM NaCl, 1 mM EDTA, 1% NP-40, 0.5% Na-deoxycholate, 0.1% SDS, 1x Complete protease inhibitor EDTA-free (Roche)) and sonicated (4 cycles of 15s ON, 15s OFF, high power) on a Bioruptor Next-Gen sonicator (Diagenode). Suspensions were centrifuged at 16000 g, 4°C for 10min Then, supernatants were collected and used as nuclear fractions. Cytoplasmic and nuclear fractions (40 µg) were separated on a 4-15% TBX-acrylamide gradient gel (Bio-Rad) and blotted onto nitrocellulose membranes. The membrane was blocked for 1 h at room temperature (1xTBS-T / 5% Milk) and cut according to expected sizes. The upper part was incubated over night at 4°C with affinity purified rabbit anti-PRDM9 (1:1000) (Grey et al., 2017) and guinea pig anti SYCP3 (1:3000) raised against mouse SYCP3 residues 24-44. Secondary antibodies were goat anti-rabbit IgG-HRP (1:5000) (1858415, Pierce) and goat anti-guinea pig IgG-HRP (1:5000) (706-035-148, Jackson Immuno Research). Blots were revealed with Super Signal West Pico Chemiluminescent Substrate, 34080, Thermo Scientific).

Yeast two-hybrid (Y2H) assay

Yeast two-hybrid experiments were performed as described previously with minor modifications (Stanzione et al., 2016). Pairwise interactions were tested in the Y2HGold Yeast strain (Cat. no. 630498, Clontech). To transform Y2HGold with bait and prey vectors, yeasts were grown in 2xYPDA medium overnight at 30^{o}C, 200 r.p.m. shaking. Afterwards, yeast cells were diluted to 0.4 optical density (measured at 600 nm) and incubated in 2xYPDA for 5 h at 30^{o}C, 200 r.p.m. shaking. Cells were harvested, washed with water and resuspended in 2 ml of 100 mM lithium acetate (LiAc). 50 µl of this cell suspension was used for each transformation. Transformation mix included 1 µg of each vector (bait and prey), 60 µl of polyethylene glycol 50% (w/v in water), 9 µl of 1.0M LiAc, 12.5 µl of boiled single-strand DNA from salmon sperm (AM9680, Ambion), and water up to 90 µl in total. The transformation mix was incubated at 30^{o}C for 30 min, and then at 42^{o}C for 30 min for the heat shock. The transformation mix was removed following centrifugation at 1000 g for 10 min, and then cells were resuspended in water, and plated first on -Leu -Trp plates to allow selective growth of transformants. After 2 days of growth, transformants were plated both on -Leu -Trp and -Leu -Trp -Ade -His plates for 2-7 days to test for interactions. We followed the manufacturer's instructions for media and plate preparation. The full length ANKRD31 protein activated the Y2H reporter system even in the absence of potential binding partner proteins from mice, which prevented the use of full length ANKRD31 in Y2H. To overcome this limitation, an array of fragments that cover the full length of ANKRD31 sequence were used in Y2H (Table S2). Self-activation tests showed that interactions could be tested

along the entire length of ANKRD31 by using a combination of ANKRD31 prey and bait constructs.

Immunofluorescence microscopy

Preparation of spermatocyte spreads

Preparation and immunostaining of nuclear surface spreads of spermatocytes was carried out according to earlier described protocols with minor modifications (Peters et al., 1997; Stanzione et al., 2016). Briefly, testis cell suspensions were prepared in PBS pH 7.4, then mixed with hypotonic extraction buffer in 1:1 ratio and incubated for 8 min at room temperature. After diluting the cell suspension five times in PBS pH 7.4, cell suspensions were centrifuged for 5 min at 1000 g, and cells were resuspended in the 1:2 mixture of PBS and 100mM sucrose solution. Cell suspensions were added to seven times higher volume droplets of filtered (0.2 µm) 1% paraformaldehyde (PFA), 0.15% Triton X-100, 1mM sodium borate pH 9.2 solution on diagnostic slides, and incubated for 60 min at room temperature in wet chambers. Nuclei were then dried for at least 1 h under fume-hood. Finally, the slides were washed in 0.4% Photo-Flo 200 (Kodak) and dried at room temperature.

Preparation of oocyte spreads

To prepare nuclear surface spread oocytes, two ovaries from each mouse were incubated in 20 µl hypotonic extraction buffer for 15 min (Hypotonic Extraction Buffer/HEB: 30 mM Tris-HCl, 17 mM Trisodium citrate dihydrate, 5 mM EDTA ,100 mM sucrose, 0.5 mM DTT, 0.5 mM PMSF, 1xProtease Inhibitor Cocktail). After incubation, HEB solution was removed and 16µl of 100 mM sucrose in 5mM sodium borate buffer pH 8.5 was added. Ovaries were punctured by two needles to release oocytes. Big pieces of tissue were removed. 9µl of 65 mM sucrose in 5 mM sodium borate buffer pH 8.5 was added to the cell suspension and incubated for 3 min. After mixing, 1.5µl of the cell suspension was added in a well containing 20µl of fixative (1% paraformaldehyde/50mM borate buffer pH:9.2/0.15% Triton-X100) on a glass slide. Cells were fixed for 45 min in humid chambers, then slides were air dried. Upon completion of drying slides were washed with 0.4% Photo-Flo 200 solution (Kodak, MFR # 1464510) for 5 min and afterwards they were rinsed with distilled water.

Immunofluorescence on gonad sections

To detect ANKRD31, testes were sectioned before fixation. Collected testes were immediately frozen in OCT (Sakura Finetek Europe) and sectioned (8 µm thick) on a cryostat. Slices of testes were allowed to dry on glass slides followed by fixation for 30 minutes at room temperature in 4% paraformaldehyde in phosphate buffer pH 7.4 followed by permeabilization in PBS/0.2%

Triton-X100 for 10min. Slides were washed in PBS 3 times, and blocked in blocking buffer (5% BSA in PBS, 0.05% tween-20, 0.05% Triton X-100) before staining with anti-ANKRD31 and anti-SYCP3 antibodies, followed by DAPI staining. Anti-SYCP3 and DAPI staining served to facilitate exact staging of prophase in spermatogonial cells.

To detect apoptosis in testis or ovary sections, we sectioned testes both before and after fixation and ovaries only after fixation. To prepare sections of gonads after fixation, testes from adults and ovaries from newborn mice were fixed in 3.6% formaldehyde in PBS pH 7.4, 0.1% Triton X-100 at room temperature for 40 min (testes) or 20min (ovaries). After fixation testes/ovaries were washed 3 times in PBS pH 7.4 and placed in 30% sucrose overnight at 4°C. Fixed testes/ovaries were frozen on dry ice in OCT (Sakura Finetek Europe). 8 µm thick sections (testes) and 5 µm thick sections (ovaries) were cut and dried onto slides. For ovary sections, an additional step of permeabilization was performed by incubating the slides for 10 min in methanol and 1 min in acetone at -20℃. The sections were washed in PBS pH 7.4 and immediately used for immunofluorescence staining. Anti-cleaved PARP staining (apoptosis marker) and histone H1t (post-mid pachytene stage marker) were detected by immunofluorescence in testes sections. DNA was counterstained by DAPI to facilitate staging of seminiferous tubules. Anti-cleaved PARP and GCNA1 (oocyte marker) (Enders and May, 1994) were detected on oocyte sections. The numbers of cleaved PARP-positive and -negative oocytes were counted on every seventh section to determine the proportion of apoptotic oocytes.

To assess oocyte numbers in adult mice DDX4 was detected in paraffin-embedded sections of ovaries in young adults (6-7weeks old). Ovaries were dissected and fixed in 4% paraformaldehyde in 100 mM Sodium Phosphate buffer pH 7.4 overnight at 4°C. Afterwards, ovaries were washed 3 times in PBS pH 7.4, once with 70% ethanol and embedded in paraffin for sectioning at 5 µm thickness. Deparaffinization and rehydration of the sections was performed as follows: 2 x 5 min in xylene, 2 x 5 min in 100% ethanol, 5 min each in 95%, 85%, 70%, 50% ethanol, 2 x 5 min in water. Sections were subjected to heat-mediated antigen retrieval in 10 mM Sodium citrate, 0.05% Tween 20, pH 6.0 for 20min on boiling water bath. Sections were permeabilized in PBS with 0.2% Triton X-100 for 45 min at room temperature and processed for immunofluorescence staining immediately. DDX4-positive oocytes were counted on every seventh section of both ovaries in each female mouse.

Staining procedures

Previously described blocking and immunostaining procedures (Stanzione et al., 2016) were optimised for immunostaining with each combination of antibodies, details are available upon request.

Quantification of immunofluorescence signal levels and focus counts

Background corrected γH2AX signal was quantified in whole nucleus with a similar strategy as described earlier (Daniel et al., 2011). DSB repair foci were counted “manually” on matched exposure images of wild type and *Ankrd31*$^{-/-}$ nuclear spreads of meiocytes. Focus numbers of pre-DSB recombinosome proteins (MEI4, REC114 and ANKRD31) and the co-localization of foci were quantified by Cell Profiler software as described previously for the analysis of MEI4, REC114 and IHO1 foci (Stanzione et al., 2016).

Immunofluorescence staining combined with pseudoautosomal region (PAR) Fluorescence *in situ* hybridization (FISH)

After 10 min wash with Washing Buffer 1 (WB1, 0.4% Photo-Flo 200, 0.01% Triton X-100 in water), surface spreads were incubated overnight at room temperature with the primary antibody diluted in antibody dilution buffer (ADB) (10% goat serum, 3% bovine serum albumin [BSA], 0.05% Triton X-100 in phosphate-buffered saline [PBS]).

Then, slides were washed in 10 min WB1 and 10 min Washing Buffer 2 (WB2 0.4% Kodak Photo-Flo 200 in water), and incubated with the secondary antibody for 60 min in a pre-warmed humidified chamber at 37°C in the dark. Following further 10 min WB1, 10 min WB2 and 1 min PBS washes, slides were incubated in Hoechst 33258/PBS solution for at least 20 min in a room temperature humidified chamber. Air-drying slides for 10 min at room temperature in the dark, coverslips were mounted using ProLong® Gold Antifade Mountant without DAPI (Molecular Probes- Life technologies cat. num. P36934). Images were captured using Leica CTR6000 Digital Inverted Microscope connected to a charge-coupled device camera and analyzed using the Leica software LAS-AF, for fluorescent microscopy.

Preparation of clone DNA and nick translation

BAC clone for PAR region (RP24500I4) were grown in standard Luria Bertani (L.B) medium at 32°C for a minimum of 16 h. DNA purification was obtained with Plasmid Maxi-Prep Kit (Qiagen). Determination of DNA concentration was made by both UV spectrophotometry at 260 nm and quantitative analysis on agarose gel. 1 µg of extracted BAC DNA was marked with fluorescent green-dUTP (Enzo Life Sciences, ref 02N32-050) using Nick Translation Kit (Abbott Molecular) according to the manufacturer’s instructions. For FISH experiment, marked probe was precipitated in EtOH 100%, 3 mM Sodium Acetate pH 5.2 and 0.1µg/µl mouse Cot-1 DNA (Invitrogen) at -80°C overnight. Resulting pellet was suspended in hybridization buffer (Enzo Life Sciences) according to the manufacturer’s instructions and denatured at 73°C for 5 min in a water bath.

PAR Fluorescence *in situ* hybridization (FISH)

Following immunofluorescence, spread slides were washed with fresh PBS at RT for 5 min, rinsed briefly in dH2O and dehydrated passing through an ethanol series and air-dried. After aging (65°C for 1 h), slides were denatured for 7 min in 70% formamide/2×SSC solution at 72°C and immediately dehydrated, passing it through −20°C cooled ethanol series and air-dried. FISH probe was applied to the slides for denaturation and hybridization steps in a humid chamber (75°C for 10 min and 37°C for at least 16 h, respectively). Following two washes with stringent wash buffer (4×SSC/0.2%Tween-20) at 55°C, slides were dehydrated through an ethanol series and air-dried. Nuclei were stained with Hoechst 33258/PBS solution for 20 min at RT and coverslips were mounted using Antifade Mountant without DAPI. Images were captured using Leica CTR6000 digital inverted microscope and analyzed using Leica software LAS-AF.

Immunofluorescence staining combined with chromosome FISH

Testes from 14 days old mice (C57BL/6J) were dissected and spread nuclei of spermatocytes were prepared as described earlier (Peters et al., 1997) with minor modifications. Briefly, a single-cell suspension of spermatogenic cells in 0.1 mM sucrose with protease inhibitors (Roche) was dropped on 1% paraformaldehyde-treated slides and allowed to settle for 3 h in a humidified box at 4°C. After brief washing with water and PBS, the spread nuclei were blocked with 5% goat serum in PBS (vol/vol), the cells were immunolabeled in a humid chamber at 4°C for 12 h with specific antibodies: anti-ANKRD31 N-terminal domain (diluted 1:400, rabbit antibody), anti-SYCP3 (1:50, mouse monoclonal antibody, Santa Cruz #74569) and anti-CENT (1:200, human – purified antibodies from human anti-centromere positive serum, Antibodies Incorporated #15-235). Secondary antibodies were used at 1:500 dilutions and incubated at 4°C for 90 min; goat anti-Rabbit IgG-AlexaFluor488 (MolecularProbes, A-11034), goat anti-Mouse IgG-AlexaFluor594 (MolecularProbes, A-11032), and goat anti-Human IgG-AlexaFluor647 (MolecularProbes, A-21445).

After the immunofluorescence staining, the slides were used for Fluorescence *in situ* hybridization (FISH) as described (Kauppi et al., 2011) with DNA FISH probes for mouse chromosomes 4, 9 and 13. Briefly, the slides were dehydrated, denatured and hybridized in a humid chamber at 37°C for 60 hours with one of three mouse chromosome painting probes with an orange emitting fluorochrome (Meta Systems probes): 1. XMP 4 orange (# D-1404-050-OR); 2. XMP 9 orange (# D-1409-050-OR); 3. XMP 13 orange (# D-1413-050-OR). After FISH, the slides were washed in stringency wash solution, drained and mounted in Vectashield-DAPI+ mounting medium.

The images were examined by Nikon Eclipse 400 microscope with a Plan Fluor objective 60x (MRH00601, Nikon) with a setup of five filter blocks: UV (Ex330-380/ Em400-420), FITC (Ex465-495/ Em505-520), ET Orange (Ex530-560/ Em580-600), Sp107/TR (Ex590-615/ Em615-645), CY5 (Ex620-660/ Em660-700). The images were captured using a DS-QiMc monochrome CCD camera (Nikon) and the NIS-Elements program (Nikon). The acquired images were processed with NIS-Elements program and saved in TIF for each channel.

Diakinesis/Metaphase I chromosome spreading

Chromosome spreads of diakinesis/metaphase I stage spermatocytes were prepared as described in (Holloway et al., 2010). Briefly, testes were decapsulated and tubules were disrupted in hypotonic buffer (1% trisodium citrate in water). Large clumps were removed and the cell suspension was incubated in hypotonic buffer for 20min at room temperature. Cell suspension was centrifuged at 200g for 10min and supernatant was removed. Afterwards, cells were fixed in a methanol/acetic acid/chloroform (3:1:0.05 ratio) fixative, centrifuged and resuspended in ice-cold methanol/acetic acid solution (3:1 ratio). Fixed cells were dropped onto slides, dried quickly (in humid conditions), and stained with Hoechst 33342.

XY chromosome painting in metaphase spreads

For sex chromosome painting, probes specific for X and Y chromosomes were used (XMP X Green, XMP Y Orange, MetaSystems). FISH protocol was performed according to manufacturer's instructions.

Staging of meiotic prophase

The first meiotic prophase can be subdivided into stages by a combination of three markers, SYCP3 (chromosome axis marker), SYCP1 (SC marker) and Histone H1t (post-mid pachytene marker in spermatocytes) (Table S1, for details see also (Stanzione et al., 2016). The stages that can be distinguished by these markers are listed briefly below, for a more detailed description see (Stanzione et al., 2016). Preleptotene stage corresponds to the premeiotic DNA replication in the cell cycle of germ cells. In a previous study (Stanzione et al., 2016), we used EdU labeling in combination with SYCP3 stain to define axis morphology that characterizes preleptotene spermatocytes. Based on this earlier study we define preleptotene as a stage where hazy/punctate staining pattern of SYCP3 is observed throughout the nucleus. The next stage, leptotene, is characterized by short stretches of axes and no SC. This is a stage where recombination is initiated in wild-type. The next stage is early zygotene, which is characterized by long, yet still fragmented, axis stretches. SC is also detected in this stage in SC proficient genotypes. During late zygotene, axes of all chromosomes are fully formed but SCs are

incomplete. Cells enter pachytene when SC formation is completed in wild-type. All chromosomes are fully synapsed in pachytene oocytes. In contrast, only autosomes synapse fully and heterologous sex chromosomes synapse only in their PARs in spermatocytes. We also define a zygotene-to-pachytene transition stage for spermatocytes, where up to one autosome pair has not finished synapsis and/or sex chromosomes were still unsynapsed or about to synapse in wild-type. Sex chromosome axes, in particular X chromosome axes, are long and stretched out in this stage. Histone H1t staining is used to sub-stage pachytene. Histone H1t is absent or weak in early pachytene. Histone H1t levels are intermediate and high in mid and late pachytene, respectively. Pachytene is followed by the diplotene stage, during which axes desynapse and the SC becomes fragmented. Histone H1t levels are high in this stage in spermatocytes. In oocytes the same stages exist but histone H1t cannot be used as a staging marker. Instead the developmental time of fetuses can be used to aid staging. Most oocytes are in zygotene and mid-pachytene in foetuses 16 and 18 days postcoitum. Most oocytes are in pachytene/diplotene in newborn mice.

Staging of prophase is not straightforward in mutants that have SC defects. We used axis morphology to unequivocally define boundaries between leptotene, early zygotene and late zygotene (see Table S1). However, by itself, axis morphology cannot be used to unambiguously distinguish stages after late zygotene. This is because fully formed axis characterizes stages between late zygotene and early diplotene, and SC is not a reliable marker in cells where SC formation is incomplete. We used histone H1t levels to aid staging in spermatocytes with fully formed axes. This allowed us to unambiguously identify pre late pachytene stages by the lack of histone H1t staining. Given the delayed/defective SC formation in *Ankrd31*$^{-/-}$ mice, *Ankrd31*$^{-/-}$ spermatocytes that have fully formed axis, incomplete SC, and low histone H1t levels could correspond to late zygotene or an abnormal early pachytene. For the purpose of our study we categorised these cells as late zygotene. We note that this ambiguity does not influence our conclusions about kinetics of pre-DSB recombinosome formation, recombination initiation or DSB repair. This is because our conclusions rely on either the unambiguous differentiation between leptotene, early zygotene and late zygotene stages based on axis morphology or the unambiguous differentiation between early pachytene and late pachytene based on histone H1t staining. Given the PAR synapsis defect in *Ankrd31*$^{-/-}$ spermatocytes we defined zygotene-to-pachytene transition as a stage where up to one autosome pair is not fully synapsed in *Ankrd31*$^{-/-}$ spermatocytes. However, we note that some of these cells might be early pachytene cells with defective synapsis. Pachytene was defined as a stage where all autosomes are fully synapsed but sex chromosomes may or may not be synapsed in *Ankrd31*$^{-/-}$ spermatocytes.

Staging of mouse seminiferous tubule cross sections

Spermatogenic cells that are located in the same section of a seminiferous tubule initiate and execute meiosis on a coordinated manner in mice. Meiotic entry occurs in spermatogenic cell layers at the perimeter of seminiferous tubules. Upon progression in meiosis, spermatogenic cells move towards the lumen of tubules. Concurrently, mitotic proliferation generates a new layer of spermatogenic cells for a new wave of meiosis at the perimeter of each seminiferous tubule. The combination of repeated meiosis entry and spermatogenic cells migration to the lumen generates the so called epithelial cycle of seminiferous tubules. In mice, the seminiferous epithelial cycle has 12 well-defined stages (I-XII) which are characterized by distinct associations of premeiotic, meiotic and post meiotic spermatogenic cell layers across crossections of seminiferous tubules (Ahmed and de Rooij, 2009). As spermatogenesis progresses, each portion of seminiferous tubules transits from stage I to XII, and then to stage I to start a new cycle. Nuclear morphology and chromatin condensation patterns differ in distinct stages of the spermatogenic process, hence detection of chromatin by DAPI was used to identify spermatogenic cell associations that define distinct stages of the seminiferous epithelial cycle. In some cases we also immunostained SYCP3 (axis) or histone-H1t (marker of spermatocytes after mid pachytene) to aid staging of the epithelial cycle. Staging without molecular markers of chromosome axis and SC suggested that stage X of epithelial cycle is characterized by the combination of elongating spermatids in the lumen, a mixture of late pachytene and diplotene cells in an intermediate cell layer, and spermatocytes that transit from leptotene to zygotene in the basal layer of seminiferous tubules (Ahmed and de Rooij, 2009). Immunostaining of axis, unsynapsed axis and/or SC markers (Figure 1C, S4E and our unpublished observations) suggested that elongating spermatids are present mostly in combination with diplotene and zygotene cells in our strain background. Hence we labeled basal and intermediate cell layers as zygotene and diplotene in Figure 1C and S4E.

Stage XII seminiferous tubules have late zygotene spermatocytes in the basal cell layer, spermatocytes undergoing meiotic divisions in the intermediate cell layer, and advanced elongated spermatids in the lumen. In contrast, the basal layer of stage I-IV tubules have early pachytene cells and increasing numbers of intermediate spermatogonia as tubules progress from stage I to IV. Stage I-IV tubules contain early round spermatids in the intermediate layer and advanced elongated spermatids in the luminal layer. Chromatin and SYCP3 staining appear similar in late zygotene and early pachytene cells. Hence it is difficult to distinguish stage XII from stage I based on spermatocytes in the basal cell layer. Spermatogonia numbers and morphology are also similar at these stages. The main distinguishing feature of stage XII is the

presence of metaphase I to anaphyse II stage spermatocytes. However, *Ankrd31*$^{-/-}$ spermatocytes fail to progress beyond metaphase I efficiently, hence intermediate and luminal cell layers cannot be used to unambiguously distinguish seminiferous tubules in stage XII and stage I in *Ankrd31*$^{-/-}$. We referred to seminiferous tubules that contained metaphase I spermatocytes as "stage XII-like" in *Ankrd31*$^{-/-}$ to indicate this ambiguity.

Quantification of unaligned chromosomes in mouse seminiferous tubule cross sections

To quantify the fraction of spermatocytes that had unaligned chromosomes we selected metaphase I spermatocytes with metaphase plates that appeared perpendicular to the plane of sectioning. We selected only cells that were clearly separable from other metaphase plates or nuclei. All the focal plains of the selected metaphase cells were inspected under microscope to ensure detection of unaligned chromosomes. We note that sectioning may have trimmed metaphase plates in some cells thereby removing unaligned chromosomes. Hence, unaligned chromosome counts from sections are underestimates of chromosome alignment defects.

Immunofluorescence-based assessment of recombination kinetics

SC formation kinetics

To assess SC formation we quantified SC formation in prophase stages that were identified based on axis morphology (Figure 3D and S5B). We focused on pre-mid pachytene stages in spermatocytes because autosomal SC defects cause spermatocyte elimination in mid pachytene (Burgoyne et al., 2009), which renders later stages of prophase unreliable for the quantification of autosomal SC defects in mutants with compromised synapsis. Hence, we quantified SC formation in juvenile mice before most spermatocytes reach mid pachytene, or we examined histone H1t (marker of post-mid pachytene stages) negative spermatocytes from adult (Figure 3D). Quantification of SC formation has limitations. Reduction in the number of cells that completed SC formation between autosomes can reflect either a kinetic delay of SC formation and/or a terminal failure of SC formation in a subpopulation of early pachytene spermatocytes. Hence, it was not possible to judge if there was a significant terminal failure in SC formation or only a kinetic delay in *Ankrd31*$^{-/-}$ spermatocytes.

DSB repair focus kinetics

To assess recombination kinetics we used immunostaining of DSB repair proteins that accumulate on the processed single-stranded DNA ends that result from DSBs (RPA, DMC1 and RAD51). This type of analysis provides information about the steady state level of recombination intermediates that are marked by the respective proteins. Thus the number of foci could vary with both the formation kinetics and the turnover of intermediates. Hence, focus

numbers do not directly reflect DSB numbers. Nonetheless, the numbers of RAD51/DMC1 foci are thought to reflect the numbers of unrepaired DNA ends that are available for homology search in the context of unsynapsed chromosome axes. RPA focus counts are thought to reflect the number of all the single-stranded DNA ends that are participating in recombination both in the context of unsynapsed and synapsed chromosome axes.

Gene expression analysis

In order to test the effect of *Ankrd31* deficiency in mouse testicular transcriptome total RNAs from *Ankrd31*$^{+/+}$ and *Ankrd31*$^{-/-}$ juvenile testes (12 days old) were extracted. RNA was extracted using RNeasy Mini (Qiagen, Cat No./ID: 74104) according to manufacturer's instructions. Quantification and quality control of RNA was performed using Agilent 2100 Bioanalyzer. mRNA was isolated from 300 ng total RNA by poly-dT enrichment followed by strand specific RNA-Seq library preparation (Ultra II Directional RNA Library Prep, NEB) following the manufacturer's instructions. Libraries were equimolarly pooled and subjected to 76 bp single end sequencing on a NextSeq 500 and Hiseq 2500 sequencer (Illumina) resulting in on average 29 Mio reads/sample (Bray et al., 2016; Kim et al., 2013).

Identification of Ankrd31 by transcriptome analysis

To screen for genes that are preferentially expressed in gonads, we profiled transcriptomes of embryonic female gonads, adult testes and an array of 17 somatic tissues from adult mice by RNA-sequencing of total RNAs. RNeasy Mini kit (Qiagen, Cat No./ID: 74104) was used according to manufacturer's instructions to purify total RNA from testes of adult mice and ovaries from fetal mice (C57/BL6xDBA/2 background). RNA was purified from ovaries that were pooled from 34-44 fetuses/newborn mice at six developmental timepoints, 11.5, 12.5, 14.5, 16.5, 18.5 and 20.5 days post coitum. Total RNA samples from mouse somatic tissues were purchased via Ambion (liver, brain, thymus, heart, lung, spleen and kidney, Cat#7800) and Zyagen (mammary gland, pancreas, placenta, salivary gland, skeletal muscle, skin, small intestine, spinal cord, tongue and uterus, Cat#MR-010). Total RNA from the listed 17 somatic tissues were mixed in equal proportions to create a somatic RNA mix, and total RNAs from testes were mixed with this somatic RNA mix in 1:17 ratio to create a testis+somatic RNA mix. mRNAs were isolated from 300 ng total RNA by poly-dT enrichment followed by strand specific RNA-Seq library preparation (Ultra II Directional RNA Library Prep, NEB) following the manufacturer's instructions. Libraries were subjected to 75 bp single end sequencing on a NextSeq 500 (Illumina) (Kim et al., 2013).

We used the ovarian RNA-seq libraries as a starting point to identify previously unannotated protein-coding genes that were specifically expressed in reproductive tissues. This screen was

based on the assumption that some of the meiosis-specific genes might have evaded annotation. To identify previously unrecognised transcripts, we used the Cufflinks suite of tools (Roberts et al., 2011) to assemble the mouse transcriptome *de novo* from our own RNA-seq data of gonads and published RNA-seq datasets of a comprehensive array of mouse tissues of the ENCODE project (Consortium, 2011, 2012)(data accessible at NCBI GEO database (Edgar et al., 2002), accession GSE36025). Tophat software was used to map reads to mouse genome assembly mm10 (Kim et al., 2013). We used Cufflinks (Roberts et al., 2011) to generate transcript contigs from mapped reads. Cuffmerge (Roberts et al., 2011) was used to merge the *de novo* assembled transcripts with the Ensembl 72 mouse transcriptome and to identify putative transcripts that were not present in the Ensembl 72 annotation. Fragment per kilobase per million (fkpm) counts were calculated for each transcript by the Cufflinks suite. The Emboss tool "getorf" was used to predict open reading frames (ORFs) in these putative transcripts (Rice et al., 2000), and InterProScan was used to identify conserved domains in the resulting predicted ORFs (Jones et al., 2014). We applied a complex set of criteria to identify genes that are potentially involved in processes related to meiotic recombination. First, we focused on transcripts whose expression peaked either in 14.5 or 16.5 days post coitum ovaries, and whose average expression was at least two times higher at these stages than in any other stage of ovary development. This criterion was chosen because leptotene to early pachytene stage oocytes, which are expected to express most of the genes involved in meiosis-specific aspects of recombination, are most abundant at 14.5 or 16.5 days post coitum. Second, we selected for transcripts whose maximum fkpm in ovaries was higher than 1, because transcripts of known meiosis–specific recombination proteins, e.g. Hormad1, Hormad2 or Iho1, were expressed well above this level. Third, any transcript of interest had to have at least ten times higher fkpm values in the transcriptome of 8-week-old testis than in the transcriptome of any non-reproductive tissues from the ENCODE project (Consortium, 2011, 2012)(NCBI GEO accession GSE36025). This criterion ensured that we primarily identified transcripts that were specific to reproductive tissue where meiosis is ongoing. We identified only six transcript contigs that matched all three criteria. Three of these transcript contigs mapped to overlapping/adjacent genomic loci. These three transcripts contained ORFs that showed strong similarity to the ORF of the predicted human Ankrd31 gene. Only these three transcript contigs encoded predicted peptides with conserved domains. Since we were interested primarily in genes that were involved in conserved processes we selected the mouse equivalent of human *Ankrd31* for further functional analysis. We compared the full length human Ankrd31 transcript with our transcript contigs to define a predicted full length mouse Ankrd31 transcript and to define the exon structure of a predicted mouse Ankrd31 gene. Our prediction of a full length Ankrd31

transcript closely matched the predicted mouse Ankrd31 transcript (XM_006517797.1) of subsequent transcriptome annotations.

To illustrate the expression of the consolidated full length Ankrd31 transcript (Figure 1), we constructed a transcriptome index by using mm10 mouse reference transcriptome (Ensembl annotation version 87) and gtf_to_fasta from the TopHat2. TPM values were calculated by the software kallisto (Version 0.43.1) and the transcriptome index.

ChIP experiments

DMC1 ChIP-seq was performed as described in (Grey et al., 2017). Two testis from *Ankrd31*$^{+/+}$ and *Ankrd31*$^{-/-}$ from 6 weeks old mice were used for each replicate. Sequencing was performed on HiSeq 2500 Rapidmode 2x50b.

H3K4me3 ChIP-seq was done as described in (Diagouraga et al., 2018). Four testis from *Ankrd31*$^{+/+}$ and *Ankrd31*$^{-/-}$ from 12dpp mice were used for each replicate. Sequencing was performed on HiSeq 2500 Rapidmode 1x75b.

ChIP-seq data computational analysis

Read alignment

After quality control, H3K4me3 ChIP-seq and DMC1 ChIP-SSDS (Single Strand DNA Sequencing) reads were mapped to the UCSC mouse genome assembly build GRCm38/mm10. Bowtie2 (with default parameters) was used to map H3K4me3 ChIP-seq reads, while the previously published method (Khil et al., 2012) was used for DMC1 ChIP-SSDS reads (*i.e.* the BWA modified algorithm and a customized script, which were specifically developed to align and recover ssDNA fragments). A filtering step was then performed on aligned reads for all ChIP-seq experiments to keep non-duplicated and high-quality mapped reads with no more than one mismatch per read. When analyzing specifically the DMC1 and H3K4me3 signals covering the pseudo-autosomal region (PAR) of sex chromosome (Fig. 6F-G, Table S7), we used a read mapping performed over a customized genome which was depleted for the PAR from assembled chrY (*i.e.* only chrY:0-90745844 was included in this customized genome). This method ensured that all reads originated from either chrX- or chrY-PAR region were mapped over a unique reference sequence, preventing multimapping and thus misquantification over this region.

Identifying meiotic hotspots

To identify meiotic hotspots from biologically replicated samples in DMC1 ChIP-SSDS, we used the Irreproducible Discovery Rate (IDR) methodology, as previously described (Diagouraga et

al., 2018). This method was developed for ChIP-seq analysis and extensively used by the ENCODE and modENCODE projects (Landt et al., 2012). The framework developed by Qunhua Li and Peter Bickel's group (https://sites.google.com/site/anshulkundaje/projects/idr) was followed. Briefly, this method allows testing the reproducibility within and between replicates by using the IDR statistics. Following their pipeline, peak calling was performed using MACS version 2.0.10 with relaxed conditions (--pvalue=0.1 --bw1000 --nomodel --shift400) on each of the two replicates, the pooled dataset, and on pseudo-replicates that were artificially generated by randomly sampling half of the reads twice for each replicate and the pooled dataset. Then IDR analyses were performed and reproducibility was checked. Final peak sets were built by selecting the top N peaks from pooled datasets (ranked by increasing p values), with N defined the highest value between n_1 (the number of overlapping peaks with an IDR below 0.01, when comparing pseudo replicates from pooled datasets) and n_2 (the number of overlapping peaks with an IDR below 0.05, when comparing the true replicates), as recommended for the mouse genome.

Signal normalization and quantitative analysis

All read distributions and signal intensities presented in this work were then calculated after pooling reads from both replicates. DMC1 ChIP-SSDS peaks were re-centered and read enrichment was normalized to the local background, as previously described (Brick et al., 2012). DMC1 ChIP-SSDS read enrichments could not be normalized between *Ankrd3*$^{+/+}$ and *Ankrd31*$^{-/-}$ mice. Indeed, the previously reported method to normalize such data (that is to consider that the total DMC1 signal should be the same between genotypes□; (Davies et al., 2016; Diagouraga et al., 2018) cannot apply to our study as the DMC1 dynamics is altered in the mutant (see Figure 4). Thus, only relative levels between regions or hotspots should be compared between different genotypes. SSDS counts from DMC1 ChIP are dependent on DMC1 half-life on ssDNA and are normalized to library size hence they can be only used to assess distribution but not the absolute numbers of single-stranded-DNA-containing recombination intermediates. The H3K4me3 signal recovered from young mice has been normalized between *Ankrd3*$^{+/+}$ and *Ankrd31*$^{-/-}$ mice assuming, as in previous studies (Davies et al., 2016; Diagouraga et al., 2018), that the signal of a PRDM9-independent set of H3K4me3 peaks should remain unchanged in testes of fertile mice at the same meiotic stage. Normalization factors were thus calculated based on the enrichment found at a set of 29 promoters of protein-coding genes (*Mlh1, Pms2, Mnd1, Dmc1, Rad21l, Mei4, Stra8, Ctcfl, Mei1, Puf60, Eef2, Rpl38, Leng8, Setx, Eif3f, Rpl37, Psmd4, Heatr3, Chmp2a, Sycp1, Sycp2, Sycp3, Morc2b, Zfp541, Spo11, Mdh1b, Rec8, Msh4, Psmc3ip*), suggested by Davies et al (2016). H3K4me3 signal presented in the present study were thus

normalized by library size (Read per million of mapped reads; RPM) then to promoters to reach the level of *Ankrd31*$^{+/+}$.

Determination of overlapping peaks

DSB hotspots identified in *Ankrd31*$^{-/-}$ mice were assigned to B6 or default hotspots on the basis of overlapping peak centers ±200bp. As reference for B6 hotspots we used previously published DSB maps (Diagouraga et al., 2018; Grey et al., 2017; Smagulova et al., 2016) and the DSB map of *Ankrd31*$^{+/+}$ mice used in this study. As a reference for default DSB sites, we used the map of the *Prdm9*$^{-/-}$ mice (Brick et al., 2012). When necessary, DSB hotspot coordinates were converted from GRCm37/mm9 to GRCm38/mm10 using the liftOver tool (https://genome.ucsc.edu/cgi-bin/hgLiftOver). Thus, 94% of peaks could be assigned to a known DSB hotspot, whereas a small fraction (6%) of DSB hotspots could not be assigned to any of the reference hotspots and was defined as new (Fig. 6B). These new hotspots have in average a weak SSDS signal (Fig. 6C) and could be PRDM9 dependent or independent.

ANKRD31 family collection and protein sequence analysis

A Hidden Markov Model (HMM) search with the mouse ANKRD31 protein in the PFAM database (v. 31.0, March 2017, (Finn et al., 2016)) detected two ankyrin repeat regions, with 3 copies each (amino acids 467-568 and 1167-1279) with highly significant E-values (1.6e-35). To search for orthologs, we performed a NCBI blastp search within the complete set of UniProt reference proteomes or the NCBI non-redundant protein database, restricting the query to the region c-terminal of the last ankyrin repeat (amino acids 1280-1856) (Sayers et al., 2011). The Ankrd31 protein family is well conserved within vertebrates and orthologs can be collected in reciprocal blasts by applying highly significant e-values (1e-10). For a multiple alignment, sequences were derived either from the UniProt database, as for the Ankrd31 orthologs of Homo sapiens (sp|Q8N7Z5|ANR31_HUMAN), Ornithorhynchus anatinus (tr|F7FXW5|F7FXW5_ORNAN), and Xenopus tropicalis (tr|F6ZDM1|F6ZDM1_XENTR), or from the NCBI protein database, as for Canis lupus familiaris (ref|XP_022272501.1|), Mus musculus (ref|XP_006517860.1|), Columba livia (ref|XP_021147901.1|), Chrysemys picta bellii (ref|XP_023960269.1|), Struthio camelus australis (ref|XP_009686903.1|), Callorhinchus milii (ref|XP_007903536.1|), and Takifugu rubripes (ref|XP_011613543.1|). Multiple alignment was performed with MAFFT (-linsi v7.313, (Katoh and Toh, 2008)), and visualized with ClustalX (v2.1,(Thompson et al., 1997)). 5 conserved regions were identified. The first ankyrin repeat region is missing in bony fish, but present in shark, whereas the second ankyrin repeat region is highly conserved in all vertebrate orthologs. The third conserved region CR3 includes a predicted coiled coil interaction domain (in

mouse ANKRD31 from 1340 to 1374 (Lupas et al., 1991)). For the conserved regions CR4 (1701-1787) and CR5 (1811-1857) no function could be assigned.

QUANTIFICATION AND STATISTICAL ANALYSIS

Statistical analysis of cytological observations was done by GrapPad Prism 7. All other statistical tests were done using R version 3.3.3, if not otherwise stated. All tests and p-values are provided in the corresponding legends and/or figures.

DATA AND SOFTWARE AVAILABILITY

RNA-seq and CHIP-seq data have been deposited in NCBI's Gene Expression Omnibus (Edgar et al., 2002) and are accessible through GEO Series accession numbers GSE119410, GSE119411 and GSE126443 at the "https://www.ncbi.nlm.nih.gov/geo/query/acc.cgi?acc=" address. Raw data for figures has been deposited in Mendeley Database: http://dx.doi.org/10.17632/jfb3msz44d.1

References

Acquaviva, L., Boekhout, M., Karasu, M.E., Brick, K., Pratto, F., van Overbeek, M., Kauppi, L., Camerini-Otero, R.D., Jasin, M., and Keeney, S. (2019). Ensuring meiotic DNA break formation in the mouse pseudoautosomal region. In bioRxiv.

Ahmed, E.A., and de Rooij, D.G. (2009). Staging of mouse seminiferous tubule cross-sections. Methods Mol Biol *558*, 263-277.

Barchi, M., Mahadevaiah, S., Di Giacomo, M., Baudat, F., de Rooij, D.G., Burgoyne, P.S., Jasin, M., and Keeney, S. (2005). Surveillance of different recombination defects in mouse spermatocytes yields distinct responses despite elimination at an identical developmental stage. Molecular and cellular biology *25*, 7203-7215.

Barchi, M., Roig, I., Di Giacomo, M., de Rooij, D.G., Keeney, S., and Jasin, M. (2008). ATM promotes the obligate XY crossover and both crossover control and chromosome axis integrity on autosomes. PLoS genetics *4*, e1000076.

Bellani, M.A., Romanienko, P.J., Cairatti, D.A., and Camerini-Otero, R.D. (2005). SPO11 is required for sex-body formation, and *Spo11* heterozygosity rescues the prophase arrest of *Atm*-/- spermatocytes. J Cell Sci *118*, 3233-3245.

Bergerat, A., de Massy, B., Gadelle, D., Varoutas, P.C., Nicolas, A., and Forterre, P. (1997). An atypical topoisomerase II from Archaea with implications for meiotic recombination. Nature *386*, 414-417.

Blat, Y., Protacio, R.U., Hunter, N., and Kleckner, N. (2002). Physical and functional interactions among basic chromosome organizational features govern early steps of meiotic chiasma formation. Cell *111*, 791-802.

Bray, N.L., Pimentel, H., Melsted, P., and Pachter, L. (2016). Near-optimal probabilistic RNA-seq quantification. Nature biotechnology *34*, 525-527.
Brick, K., Smagulova, F., Khil, P., Camerini-Otero, R.D., and Petukhova, G.V. (2012). Genetic recombination is directed away from functional genomic elements in mice. Nature *485*, 642-645.
Buard, J., Barthes, P., Grey, C., and de Massy, B. (2009). Distinct histone modifications define initiation and repair of meiotic recombination in the mouse. The EMBO journal *28*, 2616-2624.
Burgoyne, P.S., Mahadevaiah, S.K., and Turner, J.M. (2009). The consequences of asynapsis for mammalian meiosis. Nat Rev Genet *10*, 207-216.
Chicheportiche, A., Bernardino-Sgherri, J., de Massy, B., and Dutrillaux, B. (2007). Characterization of Spo11-dependent and independent phospho-H2AX foci during meiotic prophase I in the male mouse. J Cell Sci *120*, 1733-1742.
Consortium, E.P. (2011). A user's guide to the encyclopedia of DNA elements (ENCODE). PLoS biology *9*, e1001046.
Consortium, E.P. (2012). An integrated encyclopedia of DNA elements in the human genome. Nature *489*, 57-74.
Daniel, K., Lange, J., Hached, K., Fu, J., Anastassiadis, K., Roig, I., Cooke, H.J., Stewart, A.F., Wassmann, K., Jasin, M*., et al.* (2011). Meiotic homologue alignment and its quality surveillance are controlled by mouse HORMAD1. Nature Cell Biology *13*, 599-U232.
Davies, B., Hatton, E., Altemose, N., Hussin, J.G., Pratto, F., Zhang, G., Hinch, A.G., Moralli, D., Biggs, D., Diaz, R*., et al.* (2016). Re-engineering the zinc fingers of PRDM9 reverses hybrid sterility in mice. Nature *530*, 171-176.
de Massy, B. (2013). Initiation of meiotic recombination: how and where? Conservation and specificities among eukaryotes. Annual review of genetics *47*, 563-599.
Di Giacomo, M., Barchi, M., Baudat, F., Edelmann, W., Keeney, S., and Jasin, M. (2005). Distinct DNA-damage-dependent and -independent responses drive the loss of oocytes in recombination-defective mouse mutants. Proc Natl Acad Sci U S A *102*, 737-742.
Diagouraga, B., Clement, J.A.J., Duret, L., Kadlec, J., de Massy, B., and Baudat, F. (2018). PRDM9 Methyltransferase Activity Is Essential for Meiotic DNA Double-Strand Break Formation at Its Binding Sites. Mol Cell *69*, 853-865 e856.
Edgar, R., Domrachev, M., and Lash, A.E. (2002). Gene Expression Omnibus: NCBI gene expression and hybridization array data repository. Nucleic acids research *30*, 207-210.
Enders, G.C., and May, J.J., 2nd (1994). Developmentally regulated expression of a mouse germ cell nuclear antigen examined from embryonic day 11 to adult in male and female mice. Developmental biology *163*, 331-340.
Finn, R.D., Coggill, P., Eberhardt, R.Y., Eddy, S.R., Mistry, J., Mitchell, A.L., Potter, S.C., Punta, M., Qureshi, M., Sangrador-Vegas, A*., et al.* (2016). The Pfam protein families database: towards a more sustainable future. Nucleic acids research *44*, D279-285.
Ghafari, F., Gutierrez, C.G., and Hartshorne, G.M. (2007). Apoptosis in mouse fetal and neonatal oocytes during meiotic prophase one. BMC developmental biology *7*, 87.
Grey, C., Baudat, F., and de Massy, B. (2018). PRDM9, a driver of the genetic map. PLoS genetics *14*, e1007479.
Grey, C., Clement, J.A., Buard, J., Leblanc, B., Gut, I., Gut, M., Duret, L., and de Massy, B. (2017). In vivo binding of PRDM9 reveals interactions with noncanonical genomic sites. Genome research *27*, 580-590.
Hayashi, K., Yoshida, K., and Matsui, Y. (2005). A histone H3 methyltransferase controls epigenetic events required for meiotic prophase. Nature *438*, 374-378.
Holloway, J.K., Morelli, M.A., Borst, P.L., and Cohen, P.E. (2010). Mammalian BLM helicase is critical for integrating multiple pathways of meiotic recombination. J Cell Biol *188*, 779-789.
Hunter, N. (2015). Meiotic Recombination: The Essence of Heredity. Cold Spring Harbor perspectives in biology *7*.

Hwang, W.Y., Fu, Y., Reyon, D., Maeder, M.L., Tsai, S.Q., Sander, J.D., Peterson, R.T., Yeh, J.R., and Joung, J.K. (2013). Efficient genome editing in zebrafish using a CRISPR-Cas system. Nature biotechnology *31*, 227-229.

Jones, P., Binns, D., Chang, H.Y., Fraser, M., Li, W., McAnulla, C., McWilliam, H., Maslen, J., Mitchell, A., Nuka, G.*, et al.* (2014). InterProScan 5: genome-scale protein function classification. Bioinformatics *30*, 1236-1240.

Katoh, K., and Toh, H. (2008). Recent developments in the MAFFT multiple sequence alignment program. Briefings in bioinformatics *9*, 286-298.

Kauppi, L., Barchi, M., Baudat, F., Romanienko, P.J., Keeney, S., and Jasin, M. (2011). Distinct properties of the XY pseudoautosomal region crucial for male meiosis. Science *331*, 916-920.

Kauppi, L., Barchi, M., Lange, J., Baudat, F., Jasin, M., and Keeney, S. (2013). Numerical constraints and feedback control of double-strand breaks in mouse meiosis. Genes & development *27*, 873-886.

Keeney, S., Giroux, C.N., and Kleckner, N. (1997). Meiosis-specific DNA double-strand breaks are catalyzed by Spo11, a member of a widely conserved protein family. Cell *88*, 375-384.

Keeney, S., Lange, J., and Mohibullah, N. (2014). Self-organization of meiotic recombination initiation: general principles and molecular pathways. Annual review of genetics *48*, 187-214.

Khil, P.P., Smagulova, F., Brick, K.M., Camerini-Otero, R.D., and Petukhova, G.V. (2012). Sensitive mapping of recombination hotspots using sequencing-based detection of ssDNA. Genome research *22*, 957-965.

Kim, D., Pertea, G., Trapnell, C., Pimentel, H., Kelley, R., and Salzberg, S.L. (2013). TopHat2: accurate alignment of transcriptomes in the presence of insertions, deletions and gene fusions. Genome biology *14*, R36.

Kumar, R., Bourbon, H.M., and de Massy, B. (2010). Functional conservation of Mei4 for meiotic DNA double-strand break formation from yeasts to mice. Genes & development *24*, 1266-1280.

Kumar, R., Ghyselinck, N., Ishiguro, K.I., Watanabe, Y., Kouznetsova, A., Hoog, C., Strong, E., Schimenti, J., Daniel, K., Toth, A.*, et al.* (2015). MEI4: a central player in the regulation of meiotic DNA double strand break formation in the mouse. J Cell Sci.

Kumar, R., Oliver, C., Brun, C., Juarez-Martinez, A.B., Tarabay, Y., Kadlec, J., and de Massy, B. (2018). Mouse REC114 is essential for meiotic DNA double-strand break formation and forms a complex with MEI4. Life Sci Alliance *1*, e201800259.

Landt, S.G., Marinov, G.K., Kundaje, A., Kheradpour, P., Pauli, F., Batzoglou, S., Bernstein, B.E., Bickel, P., Brown, J.B., Cayting, P.*, et al.* (2012). ChIP-seq guidelines and practices of the ENCODE and modENCODE consortia. Genome research *22*, 1813-1831.

Lange, J., Yamada, S., Tischfield, S.E., Pan, J., Kim, S., Zhu, X., Socci, N.D., Jasin, M., and Keeney, S. (2016). The Landscape of Mouse Meiotic Double-Strand Break Formation, Processing, and Repair. Cell *167*, 695-708 e616.

Latrille, T., Duret, L., and Lartillot, N. (2017). The Red Queen model of recombination hot-spot evolution: a theoretical investigation. Philosophical transactions of the Royal Society of London. Series B, Biological sciences *372*.

Lesecque, Y., Glemin, S., Lartillot, N., Mouchiroud, D., and Duret, L. (2014). The red queen model of recombination hotspots evolution in the light of archaic and modern human genomes. PLoS genetics *10*, e1004790.

Lupas, A., Van Dyke, M., and Stock, J. (1991). Predicting coiled coils from protein sequences. Science *252*, 1162-1164.

Mosavi, L.K., Cammett, T.J., Desrosiers, D.C., and Peng, Z.Y. (2004). The ankyrin repeat as molecular architecture for protein recognition. Protein science : a publication of the Protein Society *13*, 1435-1448.

Myers, S., Bowden, R., Tumian, A., Bontrop, R.E., Freeman, C., MacFie, T.S., McVean, G., and Donnelly, P. (2010). Drive against hotspot motifs in primates implicates the PRDM9 gene in meiotic recombination. Science *327*, 876-879.

Page, J., de la Fuente, R., Manterola, M., Parra, M.T., Viera, A., Berrios, S., Fernandez-Donoso, R., and Rufas, J.S. (2012). Inactivation or non-reactivation: what accounts better for the silence of sex chromosomes during mammalian male meiosis? Chromosoma *121*, 307-326.

Panizza, S., Mendoza, M.A., Berlinger, M., Huang, L., Nicolas, A., Shirahige, K., and Klein, F. (2011). Spo11-accessory proteins link double-strand break sites to the chromosome axis in early meiotic recombination. Cell *146*, 372-383.

Peters, A.H., Plug, A.W., van Vugt, M.J., and de Boer, P. (1997). A drying-down technique for the spreading of mammalian meiocytes from the male and female germline. Chromosome Res *5*, 66-68.

Powers, N.R., Parvanov, E.D., Baker, C.L., Walker, M., Petkov, P.M., and Paigen, K. (2016). The Meiotic Recombination Activator PRDM9 Trimethylates Both H3K36 and H3K4 at Recombination Hotspots In Vivo. PLoS genetics *12*, e1006146.

Pratto, F., Brick, K., Khil, P., Smagulova, F., Petukhova, G.V., and Camerini-Otero, R.D. (2014). DNA recombination. Recombination initiation maps of individual human genomes. Science *346*, 1256442.

Rice, P., Longden, I., and Bleasby, A. (2000). EMBOSS: the European Molecular Biology Open Software Suite. Trends in genetics : TIG *16*, 276-277.

Robert, T., Nore, A., Brun, C., Maffre, C., Crimi, B., Bourbon, H.M., and de Massy, B. (2016). The TopoVIB-Like protein family is required for meiotic DNA double-strand break formation. Science *351*, 943-949.

Roberts, A., Pimentel, H., Trapnell, C., and Pachter, L. (2011). Identification of novel transcripts in annotated genomes using RNA-Seq. Bioinformatics *27*, 2325-2329.

Royo, H., Prosser, H., Ruzankina, Y., Mahadevaiah, S.K., Cloutier, J.M., Baumann, M., Fukuda, T., Hoog, C., Toth, A., de Rooij, D.G.*, et al.* (2013). ATR acts stage specifically to regulate multiple aspects of mammalian meiotic silencing. Genes & development *27*, 1484-1494.

Sarbajna, S., Denniff, M., Jeffreys, A.J., Neumann, R., Soler Artigas, M., Veselis, A., and May, C.A. (2012). A major recombination hotspot in the XqYq pseudoautosomal region gives new insight into processing of human gene conversion events. Human molecular genetics *21*, 2029-2038.

Sayers, E.W., Barrett, T., Benson, D.A., Bolton, E., Bryant, S.H., Canese, K., Chetvernin, V., Church, D.M., DiCuccio, M., Federhen, S.*, et al.* (2011). Database resources of the National Center for Biotechnology Information. Nucleic acids research *39*, D38-51.

Smagulova, F., Brick, K., Pu, Y., Camerini-Otero, R.D., and Petukhova, G.V. (2016). The evolutionary turnover of recombination hot spots contributes to speciation in mice. Genes & development *30*, 266-280.

Smagulova, F., Gregoretti, I.V., Brick, K., Khil, P., Camerini-Otero, R.D., and Petukhova, G.V. (2011). Genome-wide analysis reveals novel molecular features of mouse recombination hotspots. Nature *472*, 375-378.

Stanzione, M., Baumann, M., Papanikos, F., Dereli, I., Lange, J., Ramlal, A., Trankner, D., Shibuya, H., de Massy, B., Watanabe, Y.*, et al.* (2016). Meiotic DNA break formation requires the unsynapsed chromosome axis-binding protein IHO1 (CCDC36) in mice. Nat Cell Biol *18*, 1208-1220.

Thompson, J.D., Gibson, T.J., Plewniak, F., Jeanmougin, F., and Higgins, D.G. (1997). The CLUSTAL_X windows interface: flexible strategies for multiple sequence alignment aided by quality analysis tools. Nucleic acids research *25*, 4876-4882.

Vrielynck, N., Chambon, A., Vezon, D., Pereira, L., Chelysheva, L., De Muyt, A., Mezard, C., Mayer, C., and Grelon, M. (2016). A DNA topoisomerase VI-like complex initiates meiotic recombination. Science *351*, 939-943.

Wojtasz, L., Daniel, K., Roig, I., Bolcun-Filas, E., Xu, H.L., Boonsanay, V., Eckmann, C.R., Cooke, H.J., Jasin, M., Keeney, S.*, et al.* (2009). Mouse HORMAD1 and HORMAD2, Two Conserved Meiotic Chromosomal Proteins, Are Depleted from Synapsed Chromosome Axes with the Help of TRIP13 AAA-ATPase. PLoS genetics *5*.

Zickler, D., and Kleckner, N. (1999). Meiotic chromosomes: integrating structure and function. Annual review of genetics *33*, 603-754.

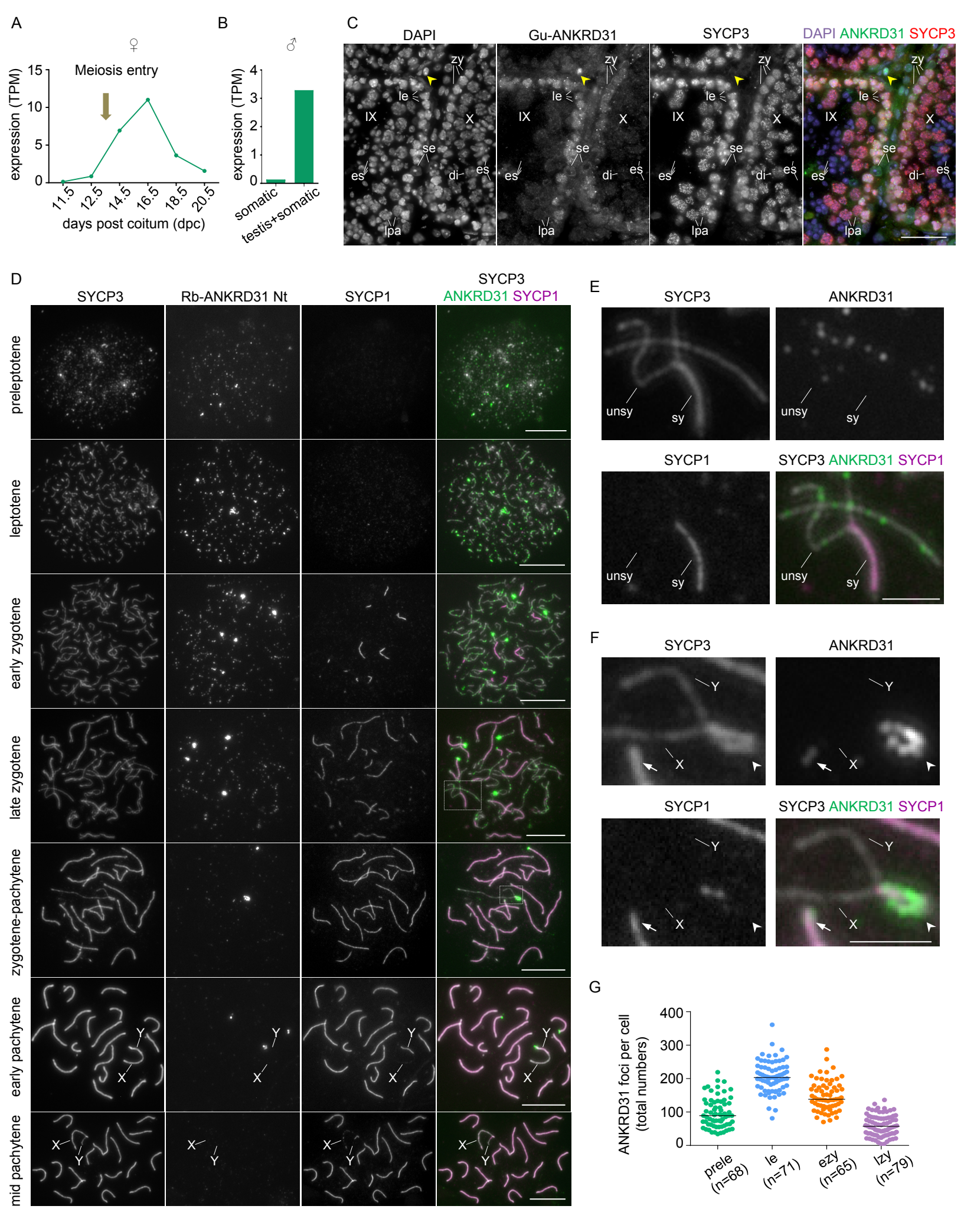
A
♀
Meiosis entry
expression (TPM)
15
10
5
0
11.5
12.5
14.5
16.5
18.5
20.5
days post coitum (dpc)
B
♂
expression (TPM)
4
3
2
1
0
somatic
testis+somatic
C
DAPI
Gu-ANKRD31
SYCP3
DAPI ANKRD31 SYCP3
zy
le
IX
X
se
es
di
es
lpa
D
SYCP3
Rb-ANKRD31 Nt
SYCP1
SYCP3
ANKRD31 SYCP1
preleptotene
leptotene
early zygotene
late zygotene
zygotene-pachytene
early pachytene
mid pachytene
Y
X
E
SYCP3
ANKRD31
unsy
sy
SYCP1
SYCP3 ANKRD31 SYCP1
F
SYCP3
ANKRD31
Y
X
SYCP1
SYCP3 ANKRD31 SYCP1
G
ANKRD31 foci per cell
(total numbers)
400
300
200
100
0
prele
(n=68)
le
(n=71)
ezy
(n=65)
lzy
(n=79)

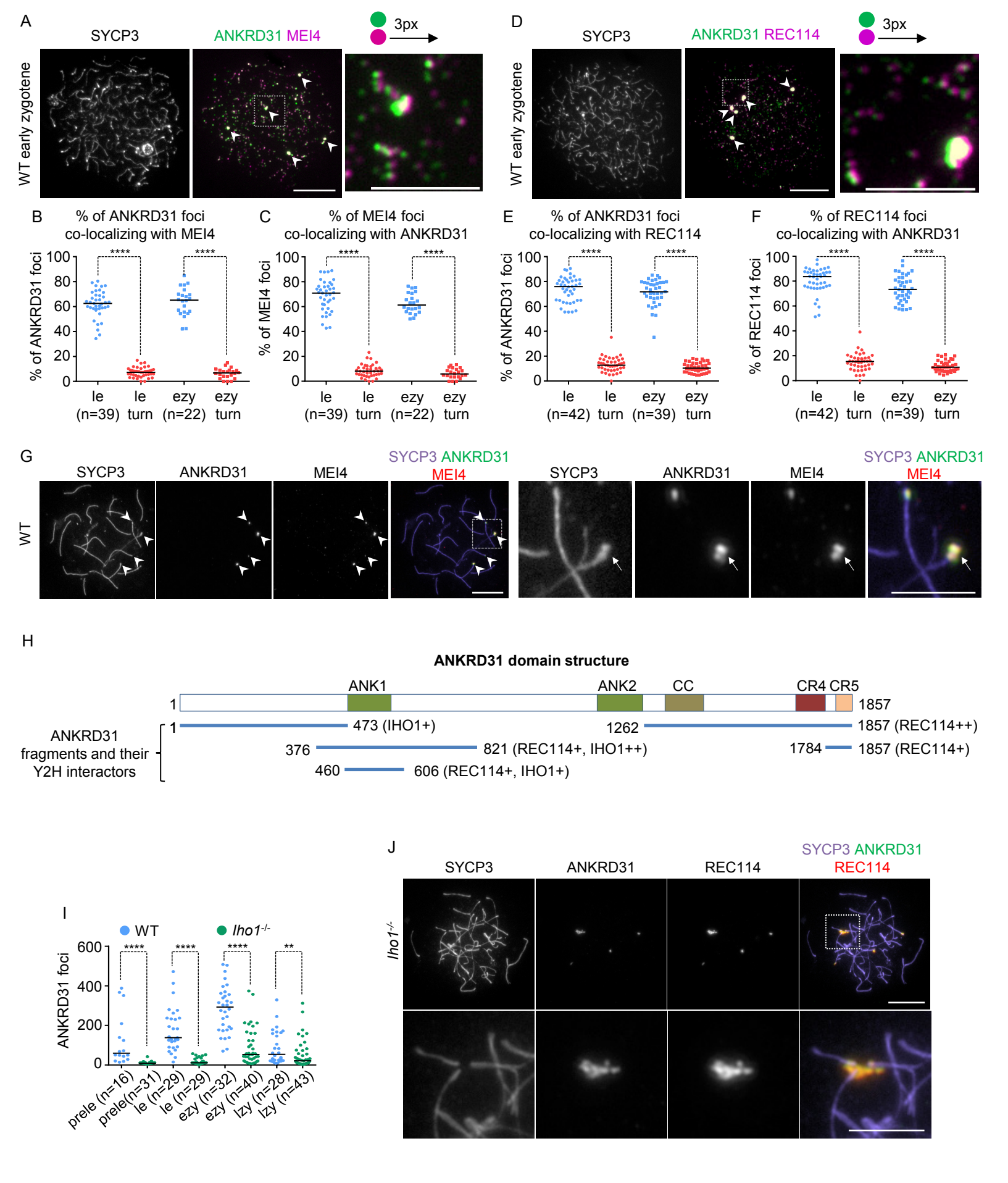
A
SYCP3
ANKRD31 MEI4
3px
WT early zygotene
D
SYCP3
ANKRD31 REC114
3px
WT early zygotene
B
% of ANKRD31 foci co-localizing with MEI4
% of ANKRD31 foci
le (n=39)
le turn
ezy (n=22)
ezy turn
C
% of MEI4 foci co-localizing with ANKRD31
% of MEI4 foci
le (n=39)
le turn
ezy (n=22)
ezy turn
E
% of ANKRD31 foci co-localizing with REC114
% of ANKRD31 foci
le (n=42)
le turn
ezy (n=39)
ezy turn
F
% of REC114 foci co-localizing with ANKRD31
% of REC114 foci
le (n=42)
le turn
ezy (n=39)
ezy turn
G
WT
SYCP3
ANKRD31
MEI4
SYCP3 ANKRD31 MEI4
H
ANKRD31 domain structure
ANK1
ANK2
CC
CR4 CR5
1
1857
ANKRD31 fragments and their Y2H interactors
1
473 (IHO1+)
1262
1857 (REC114++)
376
821 (REC114+, IHO1++)
1784
1857 (REC114+)
460
606 (REC114+, IHO1+)
I
WT
Iho1-/-
ANKRD31 foci
prele (n=16)
prele(n=31)
le (n=29)
le (n=29)
ezy (n=32)
ezy (n=40)
lzy (n=28)
lzy (n=43)
J
Iho1-/-
SYCP3
ANKRD31
REC114
SYCP3 ANKRD31 REC114

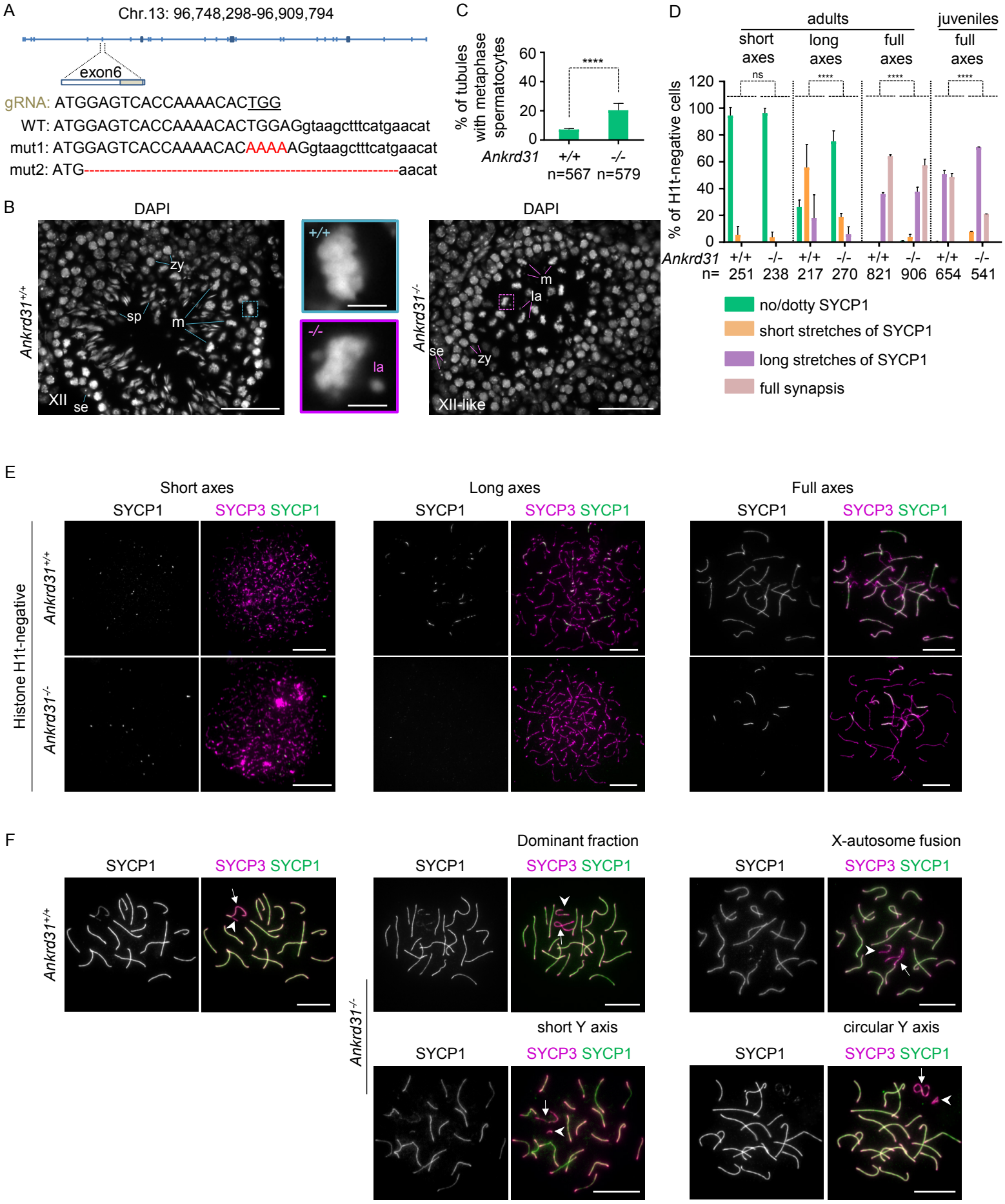
A
Chr.13: 96,748,298-96,909,794
exon6
gRNA: ATGGAGTCACCAAAACACTGG
WT: ATGGAGTCACCAAAACACTGGAGgtaagctttcatgaacat
mut1: ATGGAGTCACCAAAACACAAAAAGgtaagctttcatgaacat
mut2: ATG----------aacat
B
DAPI
Ankrd31+/+
zy
sp
m
XII
se
+/+
-/-
la
DAPI
Ankrd31-/-
m
la
se
zy
XII-like
C
% of tubules with metaphase spermatocytes
****
Ankrd31 +/+ -/-
n=567 n=579
D
adults
juveniles
short axes
long axes
full axes
full axes
% of H1t-negative cells
ns
****
Ankrd31 +/+ -/- +/+ -/- +/+ -/- +/+ -/-
n= 251 238 217 270 821 906 654 541
no/dotty SYCP1
short stretches of SYCP1
long stretches of SYCP1
full synapsis
E
Short axes
Long axes
Full axes
SYCP1
SYCP3 SYCP1
Histone H1t-negative
Ankrd31+/+
Ankrd31-/-
F
SYCP1
SYCP3 SYCP1
Ankrd31+/+
Ankrd31-/-
Dominant fraction
X-autosome fusion
short Y axis
circular Y axis

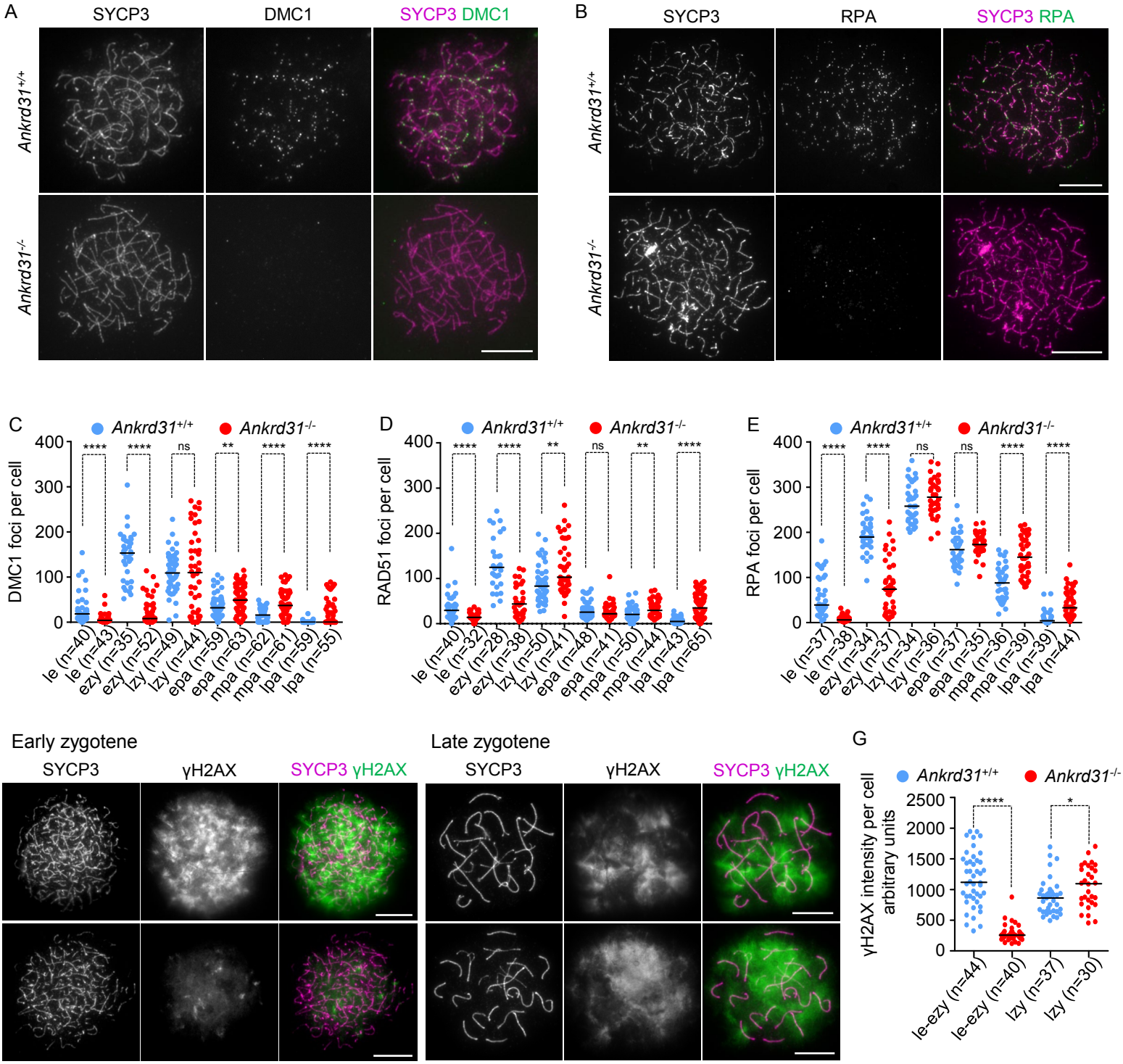
A
SYCP3
DMC1
SYCP3 DMC1
Ankrd31+/+
Ankrd31-/-
B
SYCP3
RPA
SYCP3 RPA
C
Ankrd31+/+
Ankrd31-/-
DMC1 foci per cell
le (n=40)
le (n=43)
ezy (n=35)
ezy (n=52)
lzy (n=49)
lzy (n=44)
epa (n=59)
epa (n=63)
mpa (n=62)
mpa (n=61)
lpa (n=59)
lpa (n=55)
D
RAD51 foci per cell
le (n=40)
le (n=32)
ezy (n=28)
ezy (n=38)
lzy (n=50)
lzy (n=41)
epa (n=48)
epa (n=41)
mpa (n=50)
mpa (n=44)
lpa (n=43)
lpa (n=65)
E
RPA foci per cell
le (n=37)
le (n=38)
ezy (n=34)
ezy (n=37)
lzy (n=34)
lzy (n=36)
epa (n=37)
epa (n=35)
mpa (n=36)
mpa (n=39)
lpa (n=39)
lpa (n=44)
F
Early zygotene
Late zygotene
SYCP3
γH2AX
SYCP3 γH2AX
G
γH2AX intensity per cell arbitrary units
le-ezy (n=44)
le-ezy (n=40)
lzy (n=37)
lzy (n=30)

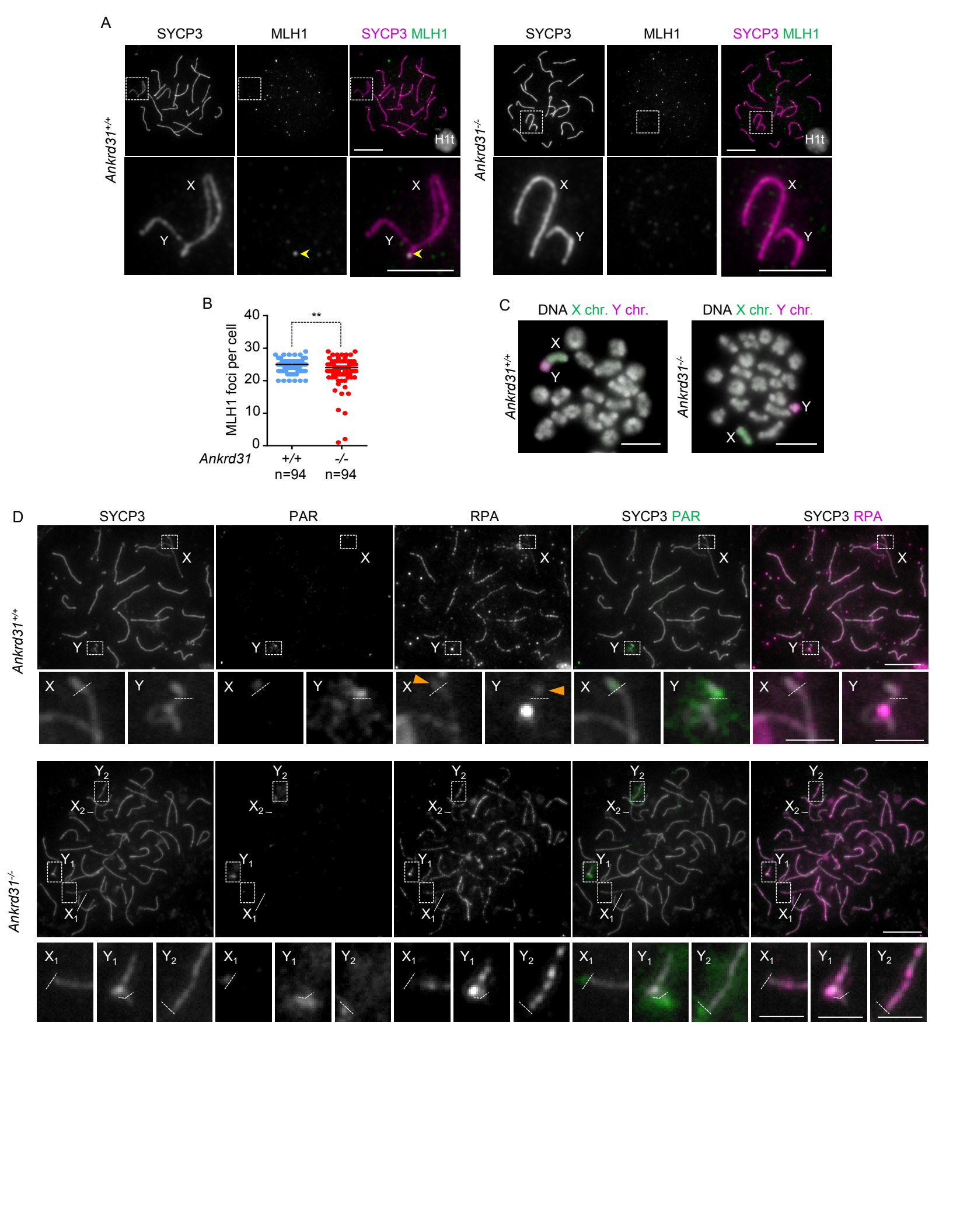
A
SYCP3
MLH1
SYCP3 MLH1
Ankrd31+/+
Ankrd31-/-
H1t
X
Y
B
MLH1 foci per cell
40
30
20
10
0
**
Ankrd31
+/+
-/-
n=94
n=94
C
DNA X chr. Y chr.
DNA X chr. Y chr.
Ankrd31+/+
Ankrd31-/-
D
SYCP3
PAR
RPA
SYCP3 PAR
SYCP3 RPA
Ankrd31+/+
Ankrd31-/-
X1
X2
Y1
Y2

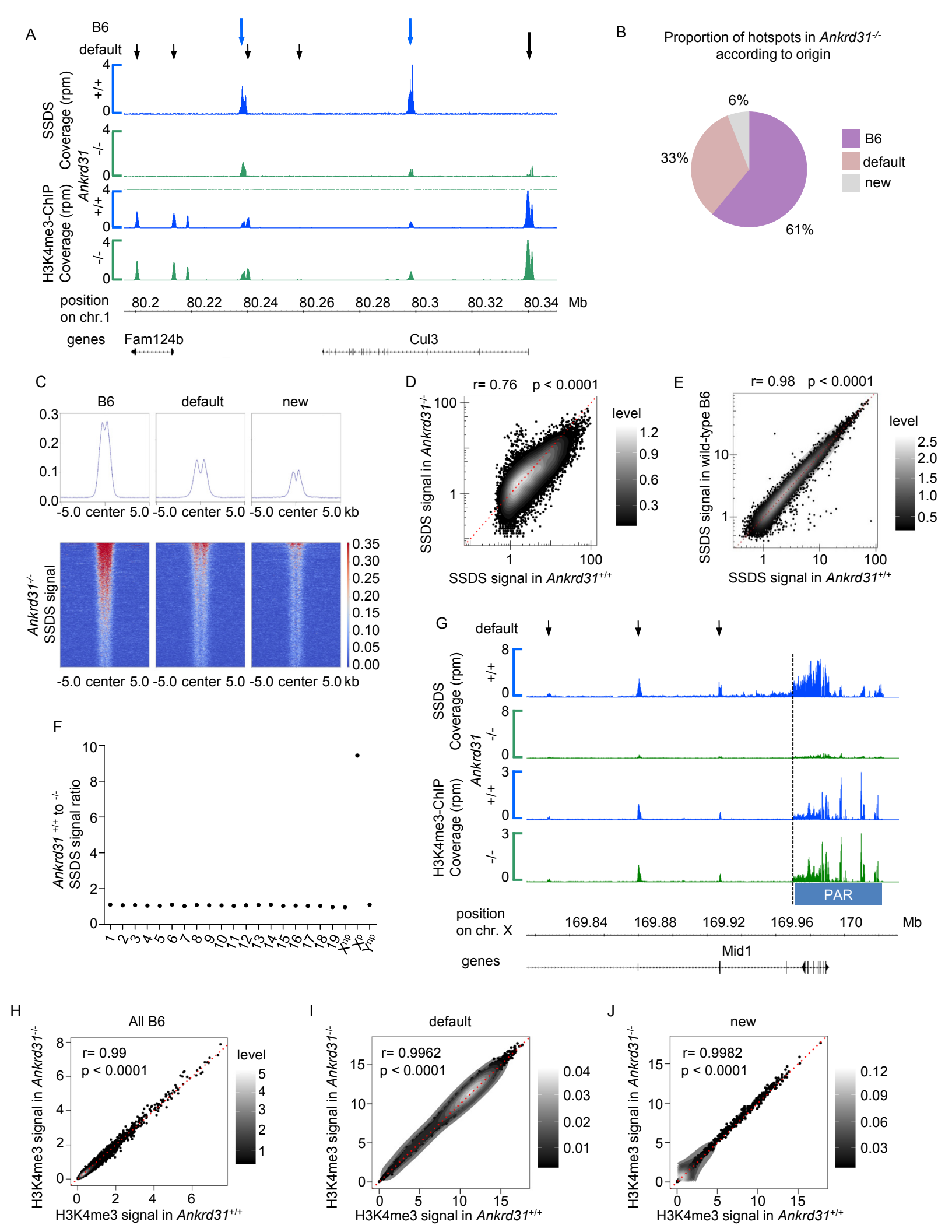
A
B6
default
SSDS Coverage (rpm)
Ankrd31
+/+
-/-
H3K4me3-ChIP Coverage (rpm)
position on chr.1
80.2 80.22 80.24 80.26 80.28 80.3 80.32 80.34 Mb
genes
Fam124b
Cul3
B
Proportion of hotspots in Ankrd31-/- according to origin
6%
33%
61%
B6
default
new
C
B6
default
new
-5.0 center 5.0 kb
Ankrd31-/- SSDS signal
D
r= 0.76 p < 0.0001
SSDS signal in Ankrd31-/-
SSDS signal in Ankrd31+/+
level
E
r= 0.98 p < 0.0001
SSDS signal in wild-type B6
SSDS signal in Ankrd31+/+
level
F
Ankrd31 +/+ to -/- SSDS signal ratio
G
default
SSDS Coverage (rpm)
H3K4me3-ChIP Coverage (rpm)
PAR
position on chr. X
169.84 169.88 169.92 169.96 170 Mb
genes
Mid1
H
All B6
r= 0.99
p < 0.0001
H3K4me3 signal in Ankrd31-/-
H3K4me3 signal in Ankrd31+/+
level
I
default
r= 0.9962
p < 0.0001
J
new
r= 0.9982
p < 0.0001

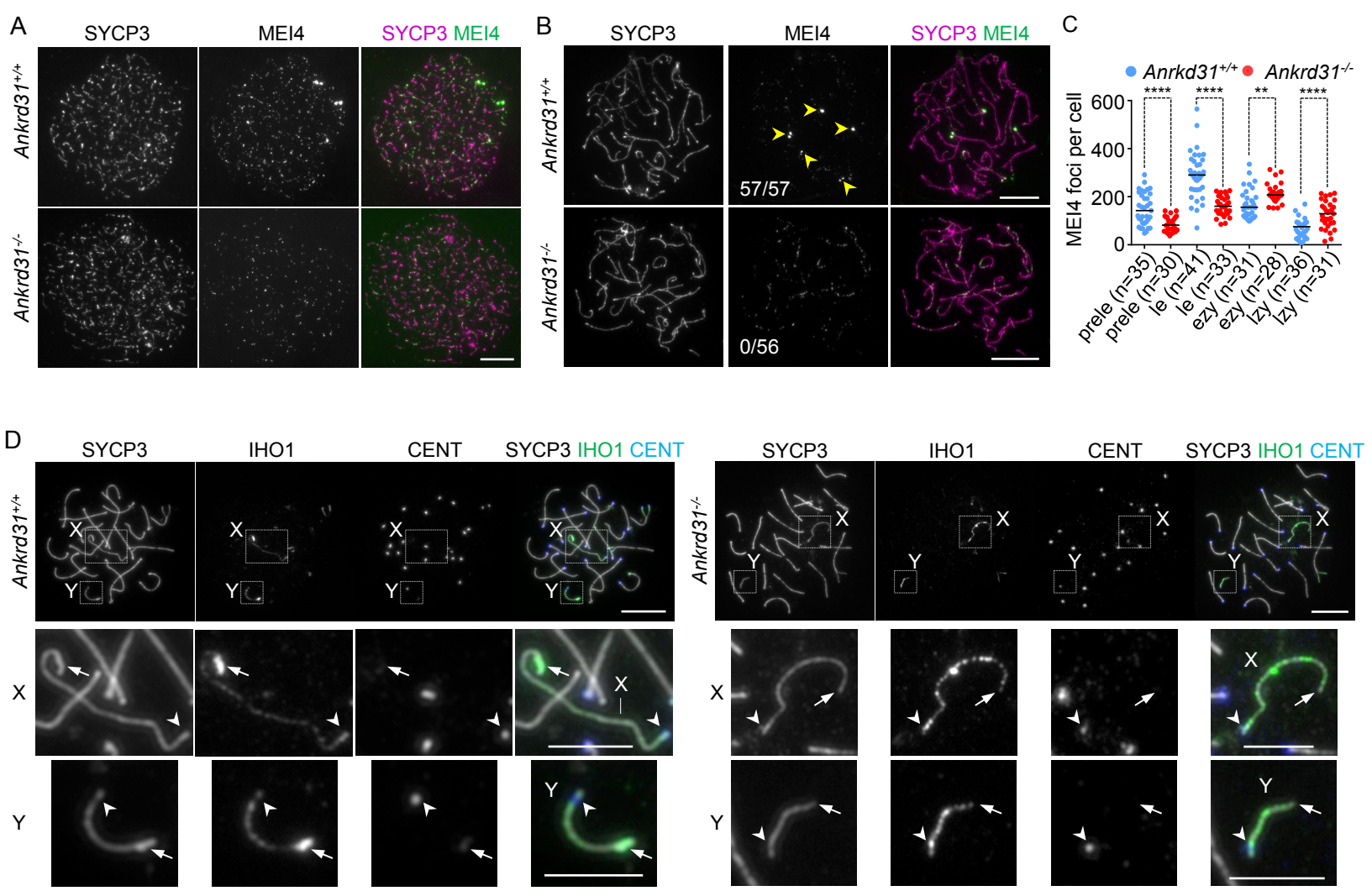
A
SYCP3
MEI4
SYCP3 MEI4
Ankrd31+/+
Ankrd31-/-
B
SYCP3
MEI4
SYCP3 MEI4
Ankrd31+/+
Ankrd31-/-
57/57
0/56
C
Anrkd31+/+
Ankrd31-/-
MEI4 foci per cell
600
400
200
0
****
****
**
****
prele (n=35)
prele (n=30)
le (n=41)
le (n=33)
ezy (n=31)
ezy (n=28)
lzy (n=36)
lzy (n=31)

D
SYCP3
IHO1
CENT
SYCP3 IHO1 CENT
Ankrd31+/+
Ankrd31-/-
X
Y

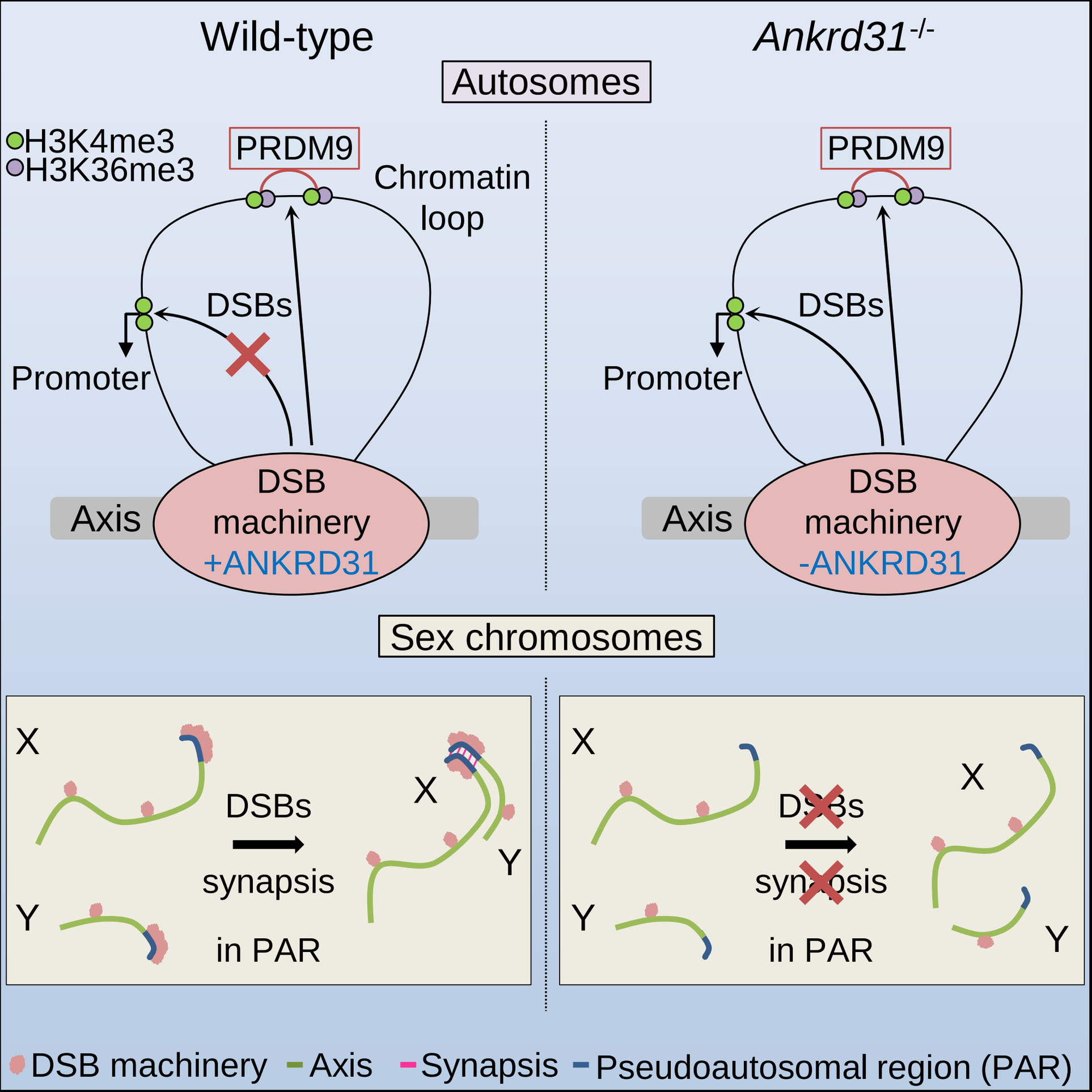
Wild-type
Ankrd31-/-
Autosomes
H3K4me3
H3K36me3
PRDM9
Chromatin loop
DSBs
Promoter
Axis
DSB machinery +ANKRD31
PRDM9
DSBs
Promoter
Axis
DSB machinery -ANKRD31
Sex chromosomes
X
Y
DSBs
synapsis
in PAR
X
Y
X
Y
DSBs
synapsis
in PAR
X
Y
DSB machinery
Axis
Synapsis
Pseudoautosomal region (PAR)